



**Applied Research and Innovation Branch**

**Hybrid A-Frame Micropile-Geosynthetic Reinforced Wall  
with Impact Barrier:  
Design Development and Construction Approach**

**by**

**Ronald Y.S. Pak, Ph.D.**

**Zhichao Zhang, Ph.D.**

**Department of Civil, Environmental & Architectural Engineering**

**University of Colorado Boulder**

**CO 80309-0428**

**Report No. CDOT-2018-11**

**November 2018**

The contents of this report reflect the views of the author(s), who is(are) responsible for the facts and accuracy of the data presented herein. The contents do not necessarily reflect the official views of the Colorado Department of Transportation or the Federal Highway Administration. This report does not constitute a standard, specification, or regulation.

1. Report No. CDOT-2018-11	2. Government Accession No.	3. Recipient's Catalog No.	
4. Title and Subtitle HYBRID A-FRAME MICROPILE-GEOSYTHETIC REINFORCED WALL WITH IMPACT BARRIER: DESIGN DEVELOPMENT AND CONSTRUCTION APPROACH		5. Report Date 5-15-2018	
		6. Performing Organization Code	
7. Author(s) Ronald Y.S. Pak and Zhichao Zhang		8. Performing Organization Report No. CDOT-2018-11	
9. Performing Organization Name and Address Department of Civil, Environmental & Architectural Engineering University of Colorado Boulder, CO 80309-0428		10. Work Unit No. (TRAIS)	
		11. Contract or Grant No. 214.03	
12. Sponsoring Agency Name and Address Colorado Department of Transportation - Research 4201 E. Arkansas Ave. Denver, CO 80222		13. Type of Report and Period Covered Final	
		14. Sponsoring Agency Code	
15. Supplementary Notes Prepared in cooperation with the US Department of Transportation, Federal Highway Administration			
16. Abstract This report presents the results of a comprehensive evaluation of a hybrid A-frame micropiles-geosynthetic reinforced soil wall design to support roadways with TL-4 impact road barriers on mountainous roads and its accompanying engineering options in dealing with the foundation stability problems in road widening and construction projects. Extensive numerical simulations of MSE walls were conducted by 3D nonlinear computer modeling using an advanced finite element code and an elastoplastic soil model that has been well calibrated in past NCHRP and CDOT projects. Collaborated partially by an experimental scaled model study that substantiated the general applicability of the modeling platform, the performance of the hybrid design under self-weight, surcharge and dynamic impacts was investigated in detail and compared with that of a truncated GRS wall with regular construction. The available option of using the A-frame micropile as an integrated solution to the related local slope-foundation stability problem that can be triggered by the wall construction was explored and quantified by the large-deformation analysis with the aid of the new threshold effective strain concept whose validity was demonstrated against ordinary limit-equilibrium slope stability methods in benchmark settings. While there remains engineering details to be explored and more realistic representation of material components to be incorporated, the study has shown that the hybrid wall design offers potential as a new or remedial engineering option in coping with difficult hillside or steep terrain conditions for road expansion or new projects. <b>Implementation:</b> The design worksheets should be further evaluated and checked for field construction, monitoring and adaptations. More refined and detailed modeling of the hybrid design's material components beyond the soil and geofabric and the performance of the system at new MASH loads is also strongly recommended.			
17. Keywords geosynthetic reinforced soil (GRS), mechanically stabilized earth (MSE), micropiles, impact road barriers, slope stability, factor of safety, finite element, large deformation, LS-DYNA		18. Distribution Statement This document is available on CDOT's website <a href="http://www.coloradodot.info/programs/research/pdfs">http://www.coloradodot.info/programs/research/pdfs</a>	
19. Security Classif. (of this report) Unclassified	20. Security Classif. (of this page) Unclassified	21. No. of Pages	22. Price

**Final Project Report for Research Project 214-03**

**Hybrid A-Frame Micropile-Geosynthetic Reinforced Wall  
with Impact Barrier:  
Design Development and Construction Approach**

by

**Ronald Y.S. Pak, Ph.D.**

**Zhichao Zhang, Ph.D.**

**Department of Civil, Environmental & Architectural Engineering  
University of Colorado Boulder  
CO 80309-0428**

**May 15, 2018**

**CDOT PROJECT COORDINATOR:**

**Aziz Khan, Ph.D., P.E.**

**CDOT TECHNICAL PANEL LEADER:**

**Trever Wang, Ph.D., P.E.**

## **ACKNOWLEDGEMENTS**

The authors like to thank CDOT's DTD Applied Research and Innovation Branch for funding and support of this study. The Study Panel includes Trever Wang, Aziz Khan, Rich Griffith, Daniel Alzamora, Teddy Meshesha, Mike Mohseni, Ryan Sullivan, Ilyess Ksouri, and Richard Wieden. Their input and suggestions throughout the project are gratefully acknowledged.

## **EXECUTIVE SUMMARY**

This report presents the results from a research project to evaluate the hybrid use of A-frame micropiles and mechanically stabilized earth (MSE) in the form of geosynthetic reinforced soil (GRS) to support roadways with impact road barriers on mountainous roads, as well as its potential to increase the local stability of a steep slope for the extra wall loading in road widening and construction projects. The design involves the installation of a pair of vertical and inclined micropiles in the form of a structural A-frame through the backfill of a highway GRS wall into the foundation base with chosen embedment. Pile caps and grade beams are then placed on the pile top upon which road barriers are connected. To evaluate the design's range of applicability and potential, extensive numerical simulations of MSE walls were conducted by 3D elastoplastic modeling using the finite element code LS-DYNA for large-deformation dynamic analysis. Adopting a constitutive soil model that has been well used and calibrated in past NCHRP and CDOT projects, a versatile computer simulation framework is developed for modeling the hybrid soil-pile-geotextile-barrier interaction problem. Collaborated by an experimental scaled model study that demonstrated the applicability of the modeling platform, the performance of the hybrid design under self-weight, surcharge and dynamic impacts was investigated in detail and compared with that of a truncated GRS wall with regular construction. The accompanying option of using the A-frame micropile as an integrated solution to the related local slope-foundation stability problem that can be triggered by the wall construction was explored and quantified by the adopted 3D finite element approach via the threshold-effective-strain concept whose applicability was demonstrated against ordinary limit-equilibrium slope stability methods in relevant 2D settings. While there remains engineering details to be explored and more realistic representation of material components to be incorporated, the study has shown that the hybrid micropile-GRS design offers appealing potentials as a new or remedial engineering option in coping with difficult hillside or steep terrain conditions for road expansion or new constructions.

## Table of Contents

1	INTRODUCTION .....	1
2	OBJECTIVES .....	3
3	APPROACH OF STUDY .....	4
4	FINITE ELEMENT MODELING OF MICROPILE A-FRAME-GRS-BARRIER- FOUNDATION DESIGN.....	6
4.1	Material Models for Soils, Geotextile, Micropiles, Barrier and Other Components in Hybrid Wall-Barrier Design .....	8
4.2	Geometric Layout of Finite Element Models for Micropile-GRS-Slope-Barrier .....	15
4.3	Experimental Confirmation of Finite Element Approach .....	22
4.4	Static and Dynamic Design Loads .....	24
5	PERFORMANCE ASSESSMENT OF HYBRID MICROPILE A-FRAME-GRS-BARRIER DESIGN .....	26
5.1	Overall Deformation of Hybrid Wall in 3 Load Stages .....	26
5.2	Lateral Earth Pressure in Basic GRS versus GRS-Micropile System.....	33
5.3	Geotextile Responses in 30m GRS and 30m GRS-Micropile Wall with 9” micropiles	35
5.4	Base Pressure under Truncated GRS .....	39
5.5	Bending Moment in Micropiles .....	40
5.6	Lateral Movement of Barrier under Impact .....	40
5.7	Lateral Displacement of GRS Front Panel.....	44
5.8	Bending Moment and Axial Load in Micropiles under Impact .....	45
5.9	Grade Beam.....	46
5.10	Soil Deformation in GRS Region .....	47
5.11	Factor of Safety and Stability of GRS and GRS-Micropile Wall on Soil Slope.....	48
5.12	Parametric Variation of Design Parameters in Hybrid Micropile A-Frame-GRS Walls	55
6	TRANSLATION OF RESEARCH TO ENGINEERING PRACTICE .....	60
7	SUMMARY AND CONCLUSIONS .....	62
8	REFERENCES .....	63

## LIST OF FIGURES

Figure 1.1: Road construction in steep slope .....	3
Figure 1.2: Micropile installation equipment.....	3
Figure 1.3: A finished roadway in mountainous areas .....	3
Figure 4.1: Yield surface definition in Geologic Cap model.....	8
Figure 4.2: Mohr-Coulomb irregular hexagon envelope and classical experimental soil data on deviatoric plane in principal stress space (Scott [25]) .....	10
Figure 4.3: Choices of approximation of Mohr-Coulomb irregular hexagon by Geological Cap or Drucker-Prager circular limit on the deviatoric plane .....	11
Figure 4.4: Stress-strain relationship of bilinear kinematic-plastic material model .....	15
Figure 4.5: Finite element models for a 6m-tall GRS-MSE walls with 3 different back slopes ..	15
Figure 4.6: Resultant displacement magnitudes of a 6m-tall GRS walls .....	16
Figure 4.7: Influence of wall height on deformability of GRS walls with 3 different backslopes	16
Figure 4.8: Vertical stress distribution near GRS base under Stage II loading: .....	17
Figure 4.9: Intermediate principal stress ratio b in GRS region .....	17
Figure 4.10: Nominal configuration of truncated GRS wall with back-slope .....	18
Figure 4.11: Concrete micropile size in terms of equivalent pile modulus in model .....	19
Figure 4.12: A single 3m-barrier segment and 30m-barrier segment of hybrid wall system .....	20
Figure 4.13: Finite element model for micropile-GRS-barrier-grade beam-anchor-foundation slope system .....	20
Figure 4.14: Impact area on finite element barrier model .....	21
Figure 4.15: Connection details of finite element model of hybrid micropile A-frame-GRS-grade beam-barrier on slope .....	21
Figure 4.16: Experimental scaled model of GRS wall with and without pile A-frame.....	23
Figure 4.17: Comparison of experimental measurements and finite element model of GRS wall with and without pile A-frame under surcharge .....	23
Figure 4.18: Load-time sequences used in Loading Stages I, II and III .....	25
Figure 5.1: Resultant displacement of 3m truncated basic GRS in Stage I-gravity: max=29.2 cm near anchor tip: foundation $\theta_{nominal}=0.2143$ .....	27
Figure 5.2: Resultant displacement of 3m GRS-pile model in Stage I-gravity: max=27.9 cm near barrier base: $\theta_{nominal}=0.2143$ , $E_{pile}=12\text{GPa}$ (9" pile).....	27
Figure 5.3: Resultant displacement of 30m truncated basic GRS under gravity: max=29.2 cm near anchor tip: foundation $\theta_{nominal} =0.2143$ .....	28
Figure 5.4: Resultant displacement of 30m GRS-pile model under gravity: max=28.1 cm near barrier: foundation $\theta_{nominal} =0.2143$ , $E_{pile}=12\text{GPa}$ (9" pile) .....	28
Figure 5.5: Cumulative resultant displacement of 3m- truncated basic GRS in Stage II-surcharge: max=34.5 cm at anchor tip: foundation $\theta_{nominal} =0.2143$ .....	29
Figure 5.6: Cumulative resultant displacement of 3m GRS-pile in Stage II-surcharge: max=31.6 cm near barrier: foundation $\theta_{nominal}=0.2143$ , $E_{pile}=12\text{GPa}$ (9" pile).....	29
Figure 5.7: Cumulative resultant displacement of 30m- truncated basic GRS in Stage II-surcharge: max=33.9 cm at anchor tip: foundation $\theta_{nominal}=0.2143$ . .....	30
Figure 5.8: Cumulative resultant displacement of 30m-GRS-pile in Stage II-surcharge: max=31.91 cm near barrier: foundation $\theta_{nominal}=0.2143$ $E_{pile}=12\text{GPa}$ (9" pile) .....	30
Figure 5.9: Cumulative resultant displacement of 3m truncated basic GRS in Stage III-dynamic impact, max>57.7 cm at barrier top: foundation $\theta_{nominal} =0.2143$ .....	31

Figure 5.10: Cumulative resultant displacement of 3m GRS-pile in Stage III-dynamic, max=34.1 cm near barrier: foundation $\theta_{\text{nominal}}=0.2143$ . $E_{\text{pile}}=12\text{GPa}$ (9" pile).....	31
Figure 5.11: Cumulative resultant displacement of 30m truncated basic GRS in Stage III-dynamic, max=40.2 cm at barrier top: foundation $\theta_{\text{nominal}}=0.2143$ .....	32
Figure 5.12: Cumulative resultant displacement of 30m GRS-pile in Stage III-dynamic, max=32.3 cm near barrier: $\theta_{\text{nominal}}=0.2143$ . $E_{\text{pile}}=12\text{GPa}$ (9" pile).....	32
Figure 5.13: Accumulated resultant displacements (magnified by 5 times) at $t=0.20$ sec under front impact of 600 kN peak load .....	33
Figure 5.14: Active, passive and at-rest earth pressure coefficients.....	33
Figure 5.15: Horizontal normal soil stress next to wall facing for 30m truncated GRS at side and mid-sections (GRS $\theta=0.1864$ , foundation $\theta=0.2143$ ).....	34
Figure 5.16: Horizontal normal soil stress next to wall facing for 30 GRS-pile case.....	35
Figure 5.17: Geotextile $\epsilon_x$ strain of 30m truncated basic GRS in Stage I-gravity (GRS $\theta=0.1864$ , foundation $\theta=0.2143$ , max=2.75% at bottom membrane edge) .....	36
Figure 5.18: Geotextile $\epsilon_x$ strain in 30m GRS with piles, $E_{\text{pile}}=12\text{GPa}$ (9" pile) in Stage I-gravity (GRS $\theta=0.1864$ , foundation $\theta=0.2143$ , max=3.08% at bottom membrane edge) .....	36
Figure 5.19: Geotextile $\epsilon_x$ strain of 30m truncated basic GRS in Stage II-surcharge (GRS $\theta=0.1864$ , foundation $\theta=0.2143$ , scale=2%), max=3.32% at bottom membrane edge, top fabric strain=0.4% .....	36
Figure 5.20: Geotextile $\epsilon_x$ strain of 30m wall with piles, $E_{\text{pile}}=12\text{GPa}$ (9" pile) in Stage II-surcharge (GRS $\theta=0.1864$ , foundation $\theta=0.2143$ , scale=2%) max=3.54% at bottom membrane edge, top fabric strain=0.3% .....	37
Figure 5.21: Geotextile $\epsilon_x$ strain of 30m truncated basic GRS in Stage III-dynamic impact (GRS $\theta=0.1864$ , foundation $\theta=0.2143$ ) max=3.4% at bottom membrane edge, top fabric strain=2% ..	37
Figure 5.22: Geotextile $\epsilon_x$ strain of 30m wall with piles, $E=12\text{GPa}$ (9" pile) in Stage III- impact (MSE $\theta=0.1864$ , foundation $\theta=0.2143$ ) max=3.6% at bottom membrane edge, top fabric strain=0.6% .....	38
Figure 5.23: Geotextile $\sigma_x$ stress in 30m truncated basic GRS in Phase III-dynamic impact on barrier: (MSE $\theta=0.1864$ , foundation $\theta=0.2143$ ).....	38
Figure 5.24: Comparison of truncated soil bearing pressure with different interfacial friction angles under gravity load.....	39
Figure 5.25: Bending moment of piles in the micropile-GRS wall with different .....	40
Figure 5.26: Horizontal barrier response of 30m MSE-12GPa, pile versus pure GRS under dynamic 240kN impact load .....	41
Figure 5.27: Effect of pile size on barrier movement upon impact in a GRS-pile system .....	42
Figure 5.28: Multiple impact load time histories on barrier .....	43
Figure 5.29: Normal and oblique impact on barrier .....	43
Figure 5.30: Comparison of barrier lateral displacement induced by.....	44
Figure 5.31: Lateral displacement of residual wall panel induced .....	45
Figure 5.32: Bending moment of micropiles induced by 600 kN impact loading in the hybrid A-frame micropile/GRS wall. ....	46
Figure 5.33: Axial force of piles induced by 600 kN impact loading.....	46
Figure 5.34: Bending moment of grade beam induced by 600 kN front impact loading .....	47
Figure 5.35: Deformation of grade beam before and after front impact.....	47
Figure 5.36: Comparison of equivalent strain in backfill region .....	48
Figure 5.37: Effective strain contour of 30m basic GRS in Stage II: .....	50

Figure 5.38: Effective strain of 30m GRS-micropile case with 2.5m pile anchorage in Stage II: foundation $\theta_{\text{marginal}}=0.176$ (Fs=1.328), $E_{\text{pile}}=14\text{GPa}$ (10'') .....	51
Figure 5.39: Effective strain of 30m GRS-micropile case with 2.5m pile anchorage in Stage II: foundation $\theta=0.176$ (Fs=1.36), $E_{\text{pile}}=14\text{GPa}$ (10'') .....	51
Figure 5.40: Effective strain of 30m basic GRS in Stage III: .....	52
Figure 5.41: Effective strain of 30m GRS-micropile case with 2.5m pile anchorage in Stage III: foundation $\theta_{\text{marginal}}=0.176$ (Fs=1.35), $E_{\text{pile}}=14\text{GPa}$ (10'') .....	52
Figure 5.42: Effective strain of 30m basic GRS in Stage III: .....	53
Figure 5.43: Effective strain of 30m micropile case with 2.5m pile anchorage in Stage III: foundation $\theta_{\text{marginal}}=0.176$ (Fs=1.35), $E_{\text{pile}}=14\text{GPa}$ (10''), Mid-plane.....	53
Figure 5.44: Effective strain near barrier of 30m basic MSE in Stage III: .....	54
Figure 5.45: Effective shear strain contour of 30m basic MSE in Stage III-dynamic: foundation $\theta_{\text{marginal}}=0.205$ (Fs=1.07) .....	54
Figure 5.46: Effective strain of 30m MSE- GRS pile case Stage III-dynamic, $E_{\text{pile}}=12\text{GPa}$ (9'') 0, 2.5m anchorage, 2.5m anchorage, foundation $\theta_{\text{marginal}}=0.176$ (Fs=1.33).....	55
Figure 5.47: Effective strain of 30m GRS pile case in Stage III-dynamic, $E_{\text{pile}}=14\text{GPa}$ (10''), 2.5m anchorage, foundation $\theta_{\text{marginal}}=0.176$ (Fs=1.35) .....	55
Figure 5.48: FS of basic GRS-slope model by LE solution via SLOPE/W.....	56
Figure 5.49: Threshold strain of basic GRS-slope model @ 19% for FS =1.159.....	56
Figure 5.50: FS and equivalent strain distribution of GRS with .....	57
Figure 5.51: FS and equivalent strain distribution of GRS with .....	58
Figure 5.52: FS and equivalent strain distribution of GRS with .....	59
Figure 6.1: CDOT Worksheet_B-504-A3.....	60
Figure 6.2: CDOT Worksheet_B-504-A5.....	61
Figure 6.3: CDOT Worksheet_B-504-V2.....	61

# 1 INTRODUCTION

For road constructions in mountainous areas with undulating terrain, complex geological setting and steep slopes, deep cuts and fills are often necessary to provide an acceptable subgrade for efficient traffic flows. Because of the continuous increase in population and interstate commerce nowadays, many highways are or will be in need of added lanes on the side of existing roads. The topography of the mountainous areas is generally characterized by river valley on one side and cliff or steep slope on the other side, with insufficient room for conventional construction and heavy equipment. In the Rocky Mountain region, the increasing frequency of having to deal with marginal slope stability problems has further aggravated the challenge in road construction. In such geotechnical settings, the earthwork required plus the eventual extra load from the built wall on the slope will incur not only high cost and risk due to difficult constructions but also the danger of triggering instability in the form of land or rock slides. In retaining wall designs for roadways, concrete cantilever retaining wall, counterfort retaining wall, anchored retaining wall and soil nail walls are conventional options. Because of their economical constructions and wide choice of soil reinforcements from geotextiles, geogrids to metal reinforcements, mechanically stabilized earth (MSE) walls have been used widely by many DOTs, including CDOT, for bridge abutments, roads and retaining walls. While they have been employed in mountainous road construction as well, normal wall configurations will usually require significant excavation into the existing slope to create a bench to support the structure and traffic loads. For slopes that are marginally stable, the necessary earthwork and the eventual heavy wall loading will increase the risk of shallow or local slope instability, and thus the feasibility of the project. From the viewpoint of minimizing the amount of excavation, a truncated MSE wall design with a vertical front face, a narrowed base and a sloping excavation that mates with the natural slope is an appealing configuration. With the requirement on the wall system to provide the necessary foundation support for impact barriers with minimum damage, however, the wall design must act not only to support the surface pavement, traffic loads as well as its self-weight, but also provide the anchorage resistance to road barriers and guard rails under vehicular impacts as required by MASH. To counter these multiple but not uncommon site and load conditions in transportation developments, new designs and remedial options that can be used to solve the problem are relevant to most DOTs. A novel idea is to install micropiles in a truncated MSE (geosynthetic reinforced soil (GRS) being an example) to add another support element that provides resistance to the impact load and to the foundation

stability. Because of the truncated geometry of the MSE, the reinforcement in the MSE will have limited layout freedom. Due to the narrow base width, the base pressure at the narrowed bottom of the MSE may become higher as a result, thereby reducing the margin of safety against foundation bearing failure. To enhance the safety of roads next to a cliff, the incorporation of micropiles in a truncated MSE wall design can be an alternative to the use of moment slabs to handle vehicular impact while serving as a reinforcement for the slope and foundation region.

These possibilities lead to CDOT's interest in a hybrid Micropile-A-Frame-Geosynthetic Reinforced Soil (GRS) wall design. The essence of the idea is to make use of a pair of vertical and inclined micropiles in the form of an A-frame and install them through the geosynthetic reinforced soil backfill of the wall into the sloping foundation with a chosen penetration depth. Structurally, the A-frame configuration of the micropiles is apt to help reduce the bending action on both piles under lateral impact loads. The possibility that the micropiles will add resistance to support the structure loads and increase the local slope stability is also one of the design's motivations. By connecting the top of the micropile A-frames to a grade beam into which impact barriers can be anchored, the hybrid design may result not only in an overall increase in the integrity of the truncated MSE wall but also stronger barrier's anchorage for roadways in mountainous construction. While MSE and micropiles have been studied and employed in many transportation projects with design guidelines ([1] - [12]), their integrated use has not seen much in-depth research or study. The closest demonstration of the potential of hybrid wall designs is the work of Pierson et al. [20-22] but it differs in that cast-in-place shafts were installed through a MSE, not micropiles. Berg and Volova [23] investigated pile driving into MSE walls and showed that the MSE-shaft system was sound and functional. Aimed at exploring the fundamental merit of the proposed system, a detailed evaluation of the approach is the goal of the study.



**Figure 1.1: Road construction in steep slope**



**Figure 1.2: Micropile installation equipment**



**Figure 1.3: A finished roadway in mountainous areas**

## **2 OBJECTIVES**

The objective of the study is to conduct a mechanistic evaluation of the performance of the idea of a hybrid micropile A-frame-GRS-foundation design with the specific choice of geotextile as the backfill reinforcement to support Type 7 or 10 Jersey barriers for TL-4 impact loading. A sound understanding of the underlying multi-component interaction and the resulting load-transfer characteristics of the integrated wall system is prudent for determining if its performance is sufficient and optimizable to meet the barrier impact demand and practical engineering requirements of truncated GRS wall systems. The study involves the evaluation of both the serviceability and ultimate limit states of the hybrid GRS wall design as well as the its potential as a new or remedial engineering option in coping with marginal hillside or steep terrain conditions.

### 3 APPROACH OF STUDY

With the number of physical components (e.g., soil, geosynthetics, concrete, and steel) in a composite material system as in a truncated GRS with micropiles with grade beam bearing on a natural slope, the use of elementary soil mechanics methods for the analysis and design of a hybrid wall system is believed to be unreliable for the proposed assessment. To provide a realistic assessment of the design's behavior as well as the mechanical interaction of the physical components within the time frame and resources of the project, it was decided that the most productive approach is to make use of (a) nonlinear finite element modeling, and (b) material models that have been used and calibrated experimentally from past CDOT's and other FHWA/DOT projects on MSE/GRS with road barriers, in lieu of site-soil specific characterizations or field testing. To implement the approach, the study proceeded in the following steps:

- Select a versatile and commonly accepted computational platform for finite element modeling
- Select relevant material models and parameters for soil, geotextile, slope, micropiles and foundation soil
- Develop and test finite element models for truncated GRS, geotextile, barrier, grad beam and micropiles
- Seek relevant experimental evidence of the appropriateness of the calibration of the micropile-GRS finite element model
- Establish static and dynamic loading conditions
- Evaluate the overall performance of hybrid micropile-GRS-barrier design
- Evaluate local performance of key components of hybrid wall system
- Consider both normal and oblique impacts on barrier
- Perform sufficient parametric simulations to provide informed options in the micropile-GRS wall design's layout for the truncated configuration
- Assist the development of engineering design and worksheets for field application

As with any structural or foundation design, the serviceability and ultimate performance states of the hybrid wall-barrier system are both important. In the present problem, the first aspect is concerned with the ability of the barrier under impact load to have limited movement so that it can be relied upon to deflect a vehicle back to the roadway. The second is concerned with the wall's

overall degree of safety and possible failure mechanisms under ultimate loading and material conditions. The first task is well suited to be evaluated by finite element modeling that can provide detailed stress and deformation information that more elementary methods cannot. As will be discussed later, the finite element code LS-DYNA that has been employed in CDOT research projects is considered most readily useful for such a task. Finding an answer to the second question by the same approach can also be achieved but it requires some additional considerations because of LS-DYNA's analytical sophistication. This refers to the capability of LS-DYNA in finding solutions for large deformation/displacement problems because of its finite-strain theoretical basis in continuum mechanics that goes beyond what ordinary small-strain finite element codes or basic rigid-plastic formulations in conventional limit equilibrium (LE) methods can handle. In particular, it has the numerical capability and realism to determine three-dimensional equilibrium states with significant distortion and geometric changes in a mechanistically consistent manner that LE and ordinary finite element methods cannot.

In commonly used limit equilibrium (LE) methods, for example, use is made of the elementary concept of shear strength and ignores the general nonlinear elastoplastic stress-strain behavior of soils. They employ rigid-body statics by dividing a potential failure wedge into vertical slices and require ad hoc assumptions on items such as inter-slice forces to achieve static determinacy and solution. In contrast, FEM does not require such a priori assumptions on failure mechanisms (the type, shape, and location of the failure surface) as it can realize incremental developments of deformation, even localization of strains, on the way to failure. This is advantageous in the analysis of a multi-material foundation or wall design such as the MSE/GRS-micropile-foundation-slope system for which reliable analytical and physical insights from prior studies are absent. The main limitation in ordinary FEM codes is that they are based on infinitesimal-strain theory. As a result, the convergence and accuracy of the solution can deteriorate as the magnitude of deformation increases. Because of its large-strain mechanics formulation, the elastoplastic finite element code LS-DYNA can provide valid solutions for a much larger range of loading when infinitesimal strain FEM would crash. Such advanced features of LS-DYNA, however, bring forth both flexibilities and complications. To evaluate the factor or margin of safety, i.e., the strength/ultimate limit state of the design, for instance, some judicious choices and definitions of what constitute failure must be first established as the code can give equilibrium solutions even when the deformation is beyond what is normally considered as failure. In the literature, there

were different proposals on how to use finite element solutions to determine the factor of safety (FS) in geotechnical-foundation engineering problems. In this study, the Shear Strength Reduction (SSR) concept [e.g., 26-30] was deemed usable to define the factor of safety for the wall and foundation aspects in combination with a newly developed ‘threshold effective strain’ concept (Pak [34]) for identifying failure mechanisms in large-deformation finite element solutions. The basic idea behind the SSR method involves finding the lowest set of Mohr-Coulomb material parameters through a reduction factor  $\eta$  under which failure is imminent, and the reciprocal of the reduction factor can then be interpreted as the factor of safety. In terms of the conventional Mohr-Coulomb friction angle  $\phi$ , the factor of safety is defined by

$$FS = \frac{1}{\eta} = \frac{\tan(\phi_{\text{nominal}})}{\tan(\phi_{\text{marginal}})} = \frac{c_{\text{nominal}}}{c_{\text{marginal}}}.$$

With the cohesion  $c$  being close to be zero for sandy and gravelly soils of interest in this study, the factor of safety FS can be effectively given by

$$FS = \frac{\tan(\phi_{\text{nominal}})}{\tan(\phi_{\text{marginal}})}.$$

#### **4 FINTE ELEMENT MODELING OF MICROPILE A-FRAME-GRS-BARRIER-FOUNDATION DESIGN**

To achieve a sound representation of the hybrid design with its multiple material components, interfacial characteristics and a variety of possible layouts, finite element modeling methodology was adopted as the investigative platform. In particular, the versatile nonlinear dynamic finite element analysis code LS-DYNA (<http://www.lstc.com/products/ls-dyna>) is chosen for this study. Its appeal includes its ability to handle large deformation and the code’s long list of built-in user options for modeling soil and structures, material modules and nonlinear contact/interface/boundary conditions, thereby allowing realistic simulation of a variety of complex soil-structure problems without intensive fundamental developments. Based on explicit time integration for fast computation to handle dynamic phenomena such as impacts and blasts, LS-DYNA has been employed in a number of DOT and FHWA/NCHRP projects including some for CDOT (e.g., NCHRP Report 663, Chang and Oncul [7], Lee [11]). A key step for a realistic finite element simulation of a physical complex soil-structure interaction system is an appropriate choice of the material models, their parameters, meshing and geometric layout. Adopting LS-

DYNA for this study offers another advantage in this regard: from its usage by past CDOT and other DOTs' projects, there exists in the literature multiple sets of experimentally calibrated soil parameters for the GRS/MSE problem via the elastoplastic Geological Cap soil model (MAT 25) as well as other material modules in LS-DYNA (e.g., see [3], [5], and Table 4.1). These experimentally validated calibrations are valuable as a useful guide for selecting the material parameters to describe the soil behavior that is most relevant to CDOT. This allows the project to avoid the need to conduct an independent experimental program to calibrate the constitutive model for the soil in the GRS or slope, which can vary from site to site.

**Table 4.1: Reference set of chosen material parameters for Geological Cap soil model**

	$\phi = 34^\circ$ soil	$\phi = 37^\circ$ soil	$\phi = 40^\circ$ soil	Retained Earth ( $\phi = 30^\circ$ )
Initial bulk modulus, K (MPa)	16.45	24.67	32.89	16.45
Initial shear modulus, G (MPa)	7.59	11.39	15.18	7.59
Failure envelope parameter, $\alpha$ (kPa)	0	0	0	0
Failure envelope linear coefficient, $\theta$	0.264	0.289	0.315	0.231
Cap surface axis ratio, R	4	4	4	4
Hardening law exponent, D (kPa) <sup>-1</sup>	$7.25 \times 10^{-6}$	$7.25 \times 10^{-6}$	$7.25 \times 10^{-6}$	$7.25 \times 10^{-6}$
Hardening law coefficient, W	2.5	1.5	1.0	2.5
Hardening law parameter, $X_0$ (kPa)	200	200	200	0

(a) Source [3]

		Simulation	McCormick Ranch Sand	NCHRP 556
Elasticity	K (MPa)	22.219	459.676	52.19
	G (MPa)	7.407	275.792	24.087
Plasticity	$\alpha$ (MPa)	4.154	0.00186	0.01
	$\beta$ (MPa <sup>-1</sup> )	0.0647	0.09718	0
	$\gamma$ (MPa)	4.055	0.00117	0
	$\theta$ (radian)	0	0.02	0.2925
Hardening Law	W	0.08266	0.064	0.023
	D (MPa <sup>-1</sup> )	0.239	0.00725	0.87
	R	28.0	2.5	4.0
	$X_0$ (MPa)	-2.819	1.20658	0.01593
Tension Cut	T (MPa)	0	-2.06843	0

(b) Source [5]

## 4.1 Material Models for Soils, Geotextile, Micropiles, Barrier and Other Components in Hybrid Wall-Barrier Design

### (a) Soil:

Soil is the major component of both the hybrid GRS-micropile system and the foundation. As noted earlier, the key to a realistic prediction of the soil deformation under loading is the constitutive model. For its balance between generality and practicality, the elastoplastic 3D Geologic Cap model (DiMaggio and Sandler 1971 [35], Hallquist 2012 [36]) as MAT 25 in LS-DYNA was adopted for the soil medium. The details of the module can be found in LS-DYNA's user's manual [32]. As a generalization of Drucker-Prager model, the key capability of the Geological Cap (GC) model has over the classical Mohr-Coulomb model is not only that it does not have the latter's corners which often creates numerical problems, but also its added ability to model plastic volumetric compaction via a movable cap on the conical yield surface. In the model, purely volumetric response is elastic until the stress point hits the cap surface, beyond which the rate of plastic volumetric strain is controlled by the hardening law. The plastic yield surface of the model consists of three regions: a shear failure envelope  $f_1(\sigma)$ , an elliptical cap  $f_2(\sigma, \kappa)$ , and a tension cutoff region  $f_3(\sigma)$ , where  $\sigma$  is the soil's stress tensor and  $\kappa$  is a hardening parameter.

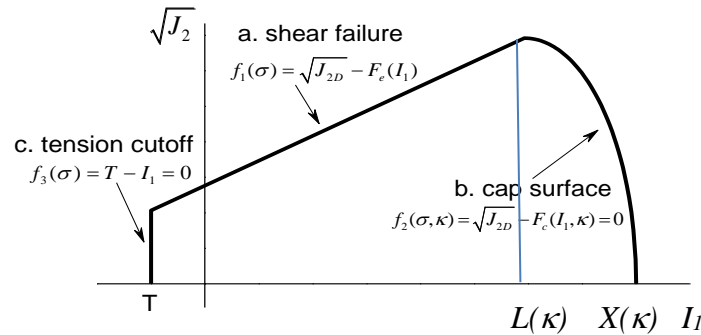


**Figure 4.1: Yield surface definition in Geologic Cap model**

The functional forms of the three surfaces are:

- a. For shear failure region where  $T \leq I_1 < L(\kappa)$ :

$$f_1(\sigma) = \sqrt{J_2} - F_e(I_1) = 0 \quad (1)$$

- b. For elliptical cap region where  $L(\kappa) \leq I_1 < X(\kappa)$ :

$$f_2(\sigma, \kappa) = \sqrt{J_2} - F_e(I_1, \kappa) = 0 \quad (2)$$

- c. For tension cutoff region where  $I_1 = T$ :

$$f_3(\sigma) = T - I_1 = 0 \quad (3)$$

where  $I_1$  is the first invariant of the stress tensor and  $J_2$  is the second invariant of the deviator stress tensor, and  $T$  is the tension cutoff value.  $F_e(I_1)$  in Eq. (1) is defined in LS-DYNA as

$$F_e(I_1) = \alpha - \gamma e^{-\beta I_1} + \theta I_1 \quad (4)$$

With  $\gamma$  and  $\beta$  set to zero in this study, Eq. (4) is reduced to

$$F_e(I_1) = \theta * I_1 + \alpha \quad (5)$$

Eq. (5) is identical to the Drucker-Prager failure criterion [37] and the parameters  $\alpha$  and  $\theta$  are comparable to the classical Mohr-Coulomb's cohesion and friction angle parameters  $c$  and  $\phi$ . The function  $F_c(I_1, \kappa)$  in Eq. (2) is defined by

$$F_c(I_1, \kappa) = \frac{1}{R} \sqrt{[X(\kappa) - L(\kappa)]^2 - [I_1 - L(\kappa)]^2} \quad (6)$$

$$X(\kappa) = \kappa + RF_e(\kappa) \quad (7)$$

$$L(\kappa) = \begin{cases} \kappa & \text{if } \kappa > 0 \\ 0 & \text{if } \kappa \leq 0 \end{cases} \quad (8)$$

with  $R$  being a shape factor that represents the ratio of major to minor axes of the elliptical cap,  $X(\kappa)$  denoting the intersection of the cap surface with the  $I_1$  axis and  $\kappa$  being a hardening parameter.

The latter is related to the plastic volume change  $\varepsilon_v^p$  through the hardening law

$$\varepsilon_v^p = W \{1 - e^{-D[X(\kappa) - X_0]}\} \quad (9)$$

where  $W$  characterizes the plastic volumetric strain's limit,  $D$  denotes the total volumetric plastic strain rate, and  $X_0$  represents the initially-set intersection of the cap surface with the  $I_1$ -axis in the stress space and defines the size of the initial elastic domain of the soil.

While the GC model has been used and calibrated in multiple DOT or NCHRP projects, it should be noted that it also has its limitations in regard to representing soil behavior fully. As shown in Fig. 4.2, experimental soil test results are generally closer to the Mohr-Coulomb irregular hexagonal shape on the deviatoric  $\pi$ -plane in the 3D principal stress space (Scott [25]), i.e., there is a dependence of the shear strength on the ratio of the major, minor as well as the intermediate principal stresses  $\sigma_1, \sigma_2$  and  $\sigma_3$ , than the pure circular locus that is assumed in the Drucker-Prager and GC models. Upon knowing the eventual failure combination of  $(\sigma_1, \sigma_2, \sigma_3)$  or its Lode's angle  $\theta_{Lode}$ , on the other hand, the shear strength parameters  $c$  and  $\phi$  of Mohr-Coulomb criterion can be

chosen analytically to give the same failure stress state via the strength parameters  $\alpha$  and  $\theta$  of the Geological Cap model. To obtain realistic predictions of the soil, such a matching criterion is important so that a representation of soil's strength via the GC model is not unconservative by overestimating its shear strength in three-dimensional problems. For a stress path that has a specific Lode's angle  $\theta_{Lode}$  which is related to the intermediate principal stress ratio  $b=(\sigma_2-\sigma_3)/(\sigma_1-\sigma_3)$ , the Mohr–Coulomb failure criterion can be expressed in terms of the stress invariants as

$$\frac{I_1}{3} \sin \varphi - \sqrt{J_2} (\cos \theta_{Lode} + \frac{1}{\sqrt{3}} \sin \theta_{Lode} \sin \varphi) + c \cos \varphi = 0 \quad (10)$$

or

$$\sqrt{J_2} = \frac{\sqrt{3} \sin \varphi}{3(\sqrt{3} \cos \theta_{Lode} + \sin \theta_{Lode} \sin \varphi)} * I_1 + \frac{\sqrt{3} \cos \varphi}{\sqrt{3} \cos \theta_{Lode} + \sin \theta_{Lode} \sin \varphi} * c \quad (11)$$

where

$$\theta_{Lode} = \frac{1}{3} \arcsin(-\frac{3\sqrt{3}}{2} \frac{J_3}{J_2^{3/2}}), \quad -\frac{\pi}{6} \leq \theta_{Lode} \leq \frac{\pi}{6}, \quad \tan \theta_{Lode} = \frac{2\sigma_2 - \sigma_1 - \sigma_3}{\sqrt{3}(\sigma_1 - \sigma_3)} = \frac{2b-1}{\sqrt{3}} \quad (12)$$

and  $J_3$  is the third deviatoric stress invariant. Setting Eq. (11) and Eq. (5) to be the same for a specific  $\theta_{Lode}$ , the Geological Cap strength parameters can be related to Mohr–Coulomb strength parameters via

$$\alpha = \frac{\sqrt{3} \cos \varphi}{\sqrt{3} \cos \theta_{Lode} + \sin \theta_{Lode} \sin \varphi} * c \quad (13)$$

$$\theta = \frac{\sqrt{3} \sin \varphi}{3(\sqrt{3} \cos \theta_{Lode} + \sin \theta_{Lode} \sin \varphi)} \quad (14)$$

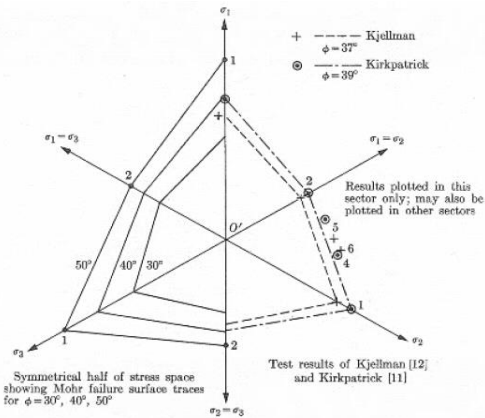
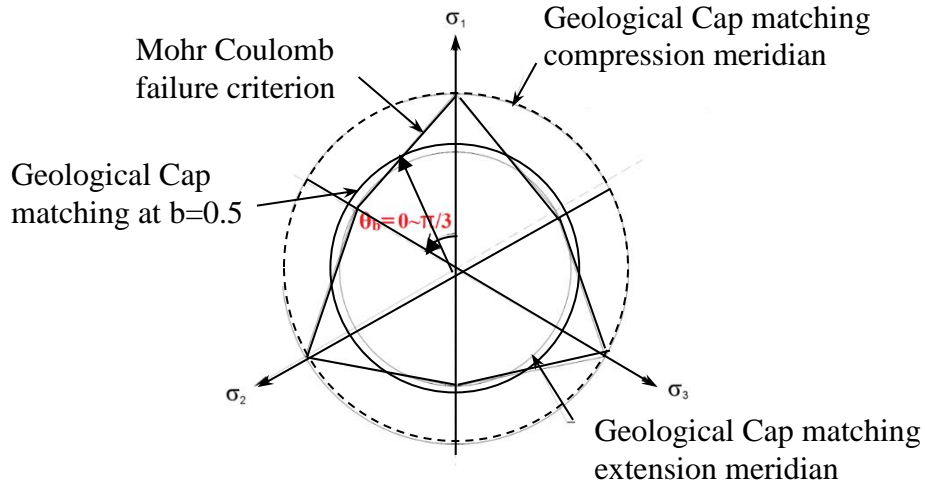


FIG. 7-8. View normal to deviatoric plane  $\sigma_1 + \sigma_2 + \sigma_3 = C$ , showing trace of Mohr-theory failure surface and test results.

**Figure 4.2: Mohr-Coulomb irregular hexagon envelope and classical experimental soil data on deviatoric plane in principal stress space (Scott [25])**



**Figure 4.3: Choices of approximation of Mohr-Coulomb irregular hexagon by Geological Cap or Drucker-Prager circular limit on the deviatoric plane**

Matching the Geological cap model's strength with Mohr-Coulomb's in the conventional triaxial compression, ( $\theta_{Lode} = -30^\circ$ ,  $b=0$ ), for example, one finds

$$\alpha = \frac{6 \cos \varphi}{\sqrt{3}(3 - \sin \varphi)} * c \quad (15)$$

$$\theta = \frac{2 \sin \varphi}{\sqrt{3}(3 - \sin \varphi)} \quad (16)$$

To match their strengths in triaxial extension ( $\theta_{Lode} = 30^\circ$ ,  $b=1$ ), the relationship is

$$\alpha = \frac{6 \cos \varphi}{\sqrt{3}(3 + \sin \varphi)} * c \quad (17)$$

$$\theta = \frac{2 \sin \varphi}{\sqrt{3}(3 + \sin \varphi)} \quad (18)$$

As will be illustrated later for the GRS wall problem in the next section, however, the stress state in the GRS soil region was found to have an intermediate stress ratio  $b$  that averages to about 0.5 from the prediction of the GC model (corresponding to  $\theta_{Lode} = 0^\circ$ ) instead of 0 or 1 (see. Fig. 4.3). To be consistent analytically, the Geological Cap model's strength parameter were thus taken to be

$$\alpha = c \cos \varphi , \quad (19)$$

$$\theta = \sin \varphi / 3. \quad (20)$$

and the resulting relationship between  $\theta$  and  $\varphi$  is given in tabulated form in Table 4.2.

**Table 4.2: Relationship between the friction angles  $\theta$  and  $\phi$  for intermediate stress ratio  $b=0.5$**

$\phi$	29°	30°	31°	32°	33°	34°	35°	36°	37°	38°	39°	40°
$\theta$	.161	.166	.171	.176	.181	.186	.191	.195	.200	.205	.209	.214
	6	7	7	6	5	4	2	9	6	2	8	3

Selected to be the focus of this study according to the field conditions of interest, sandy or gravelly soils with minimal cohesion and a friction angle of  $\phi=34^\circ$  and  $40^\circ$  were chosen as the nominal cases to consider. As indicated in Table 4.2, they correspond to  $\theta=0.186$  and  $\theta=0.2143$  in the Geological Cap model, respectively for  $b=0.5$ . For these two cases, their complete set of chosen Geological Cap soil parameters are given in Table 4.3 and 4.4, respectively.

**Table 4.3: Geological Cap Parameters for backfill soil in GRS region for  $\phi=34^\circ$  at  $b=0.5$**

Parameter	K(MPa)	G(MPa)	$\alpha$ (kPa)	$\beta$ (MPa-1)	$\gamma$ (MPa)	$\theta_{GRS}$
Value	from 16~48	from 7~22	2	0	0	0.1864
Parameter	W	D(MPa <sup>-1</sup> )	R	X <sub>0</sub> (kPa)	Tension Cutoff (MPa)	Soil density (kg/m <sup>3</sup> )
Value	2.5	0.00725	4	from 20~400kPa	0	1596

**Table 4.4: Geological Cap parameters for soil with  $\phi=40^\circ$  at  $b=0.5$**

Parameter	K(MPa)	G(MPa)	$\alpha$ (kPa)	$\beta$ (MPa-1)	$\gamma$ (MPa)	$\theta_{\text{slope}}$
Value	32.89	15.18	2.7	0	0	0.2143
Parameter	W	D(MPa <sup>-1</sup> )	R	X <sub>0</sub> (kPa)	Tension Cutoff (MPa)	Soil density (kg/m <sup>3</sup> )
Value	2.5	0.00725	4	0	0	1596

For a slope that is a soft rock, a linearly elastic model was employed with the material moduli given in Table 4.5.

**Table 4.5: Linear elastic model for soft rock**

Parameter	Density (kg/m <sup>3</sup> )	E (GPa)	$\nu$
Value	2000	3	0.3

**(b) Geotextile:**

With geotextile Amoco 20440 being recommended by CDOT as the geosynthetics of focus for the study, the bilinear kinematic-plastic model in LS-DYNA was adopted for its modeling (see Fig. 4.4) with its material parameters for the geotextile being listed in Table 4.6.

**Table 4.6: Parameters for geotextile kinematic-plastic material model**

Density	Yield stress $\sigma_y$ (MPa)	Initial elastic modulus E (MPa)	Post-yield tangent modulus E <sub>t</sub> (MPa)	Poisson's ratio $\nu$
1000	4.33	433	0 or 162	0.3

**(c) Concrete:**

Concrete elements of the system such as wall facing, barriers, grade beams and micropiles are modeled as a linear elastic material model with moduli given in Table 4.7.

**Table 4.7: Parameters for concrete by linearly elastic model**

Parameter	Density (kg/m <sup>3</sup> )	Elastic modulus E E (GPa)	Poisson ratio
Value	2320	25	0.15

**(d) Steel:**

The steel portion of the model such as dowels, rebars and anchors is likewise assumed to be linearly elastic as given in Table 4.8.

**Table 4.8: Parameters for steel dowel and rebar for bilinear kinematic-plastic model**

Parameters	Density	$\sigma_y$ (MPa)	E(GPa)	Et(GPa)
Values	7800	235	210	2

**(e) Interfacial conditions:**

Concrete material in the hybrid wall includes micropile, road barrier, grade beam and the front wall panel. The contact conditions are taken to be either tied or frictional between different materials with parameters given in Table 4.9. Bonded contact is used between micropiles and grade beam because of the expected cementation of concrete. To simulate the continuity between backfill and foundation soil, bonded contact is assumed between the backfill and foundation soil.

**Table 4.9: Interfacial friction coefficients between materials**

GRS to fdn	piles to grade beam	piles to fdn	barrier to soil	wall to soil	geotextile to soil	geotextile to wall	wall toe to fdn
Bonded	Bonded	Bonded	0.45	0.45	0.45	Tied	free

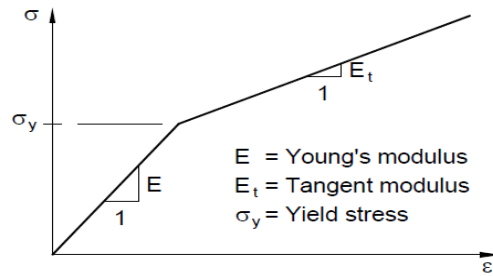


**Figure 4.4: Stress-strain relationship of bilinear kinematic-plastic material model in LS-DYNA**

#### 4.2 Geometric Layout of Finite Element Models for Micropile-GRS-Slope-Barrier

Before detailed modeling of the hybrid wall system, a preliminary finite element study of 9 basic truncated GRS configurations was conducted for 3 different heights and 3 different backslope inclinations for insights on aspects such as the deformability of truncated GRS and the failure stress condition of the soil with the geotextile reinforcement. The results are shown in Fig. 4.5 to 4.8. From the displays, one can see that the narrower base and the backslope inclination of a truncated GRS geometry, without added engineering measures to strengthen it, can indeed lead to significant deformation and higher soil bearing pressure at the base. From the output of the principal stresses in these analyses shown in Fig. 4.9, the intermediate principal stress ratio  $b$  was found to be generally between 0.4 and 0.6 in GRS region, with an average of around 0.5, which was the basis of the development of Eqn. 19 and 20 as noted earlier.

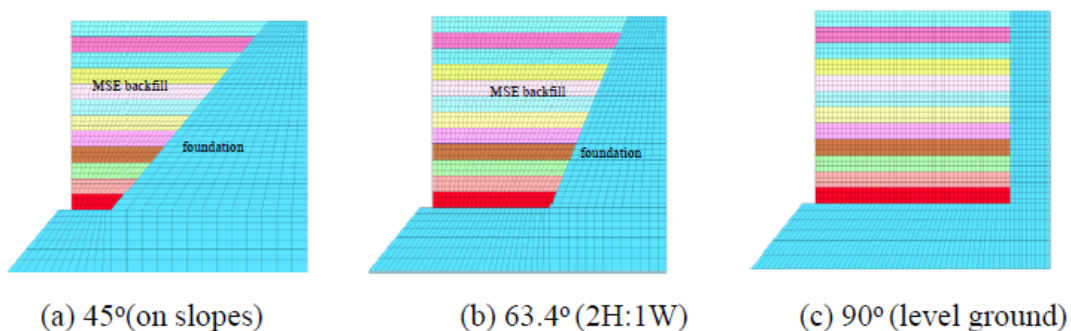


**Figure 4.5: Finite element models for a 6m-tall GRS-MSE walls with 3 different back slopes**

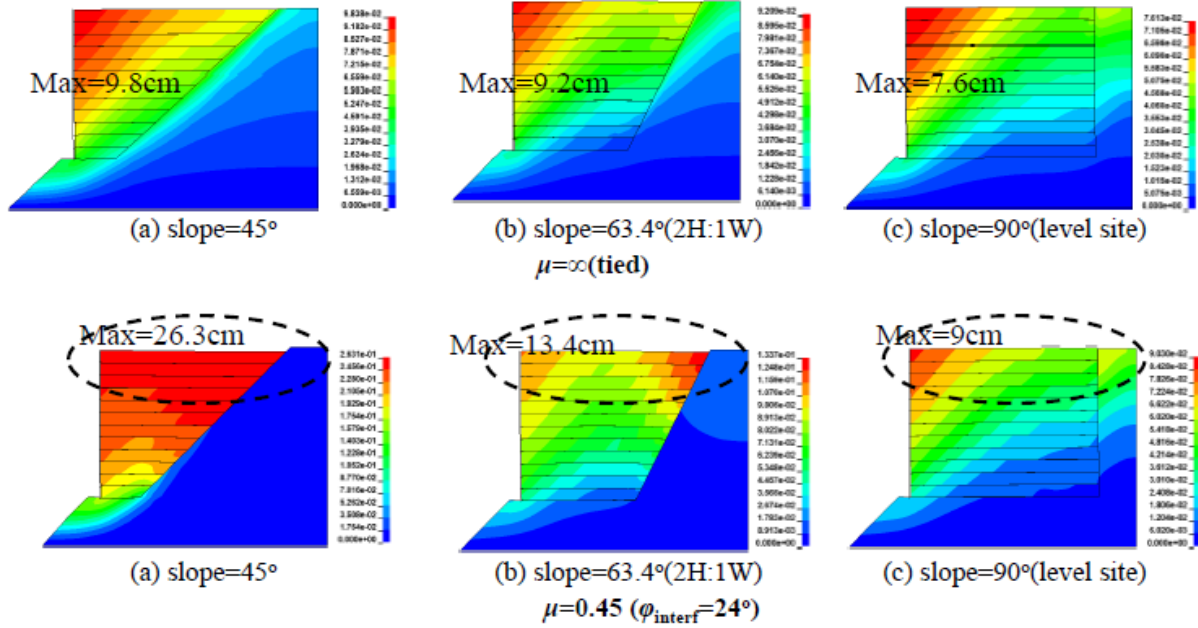


Figure 4.6: Resultant displacement magnitudes of a 6m-tall GRS walls with 3 different back slopes

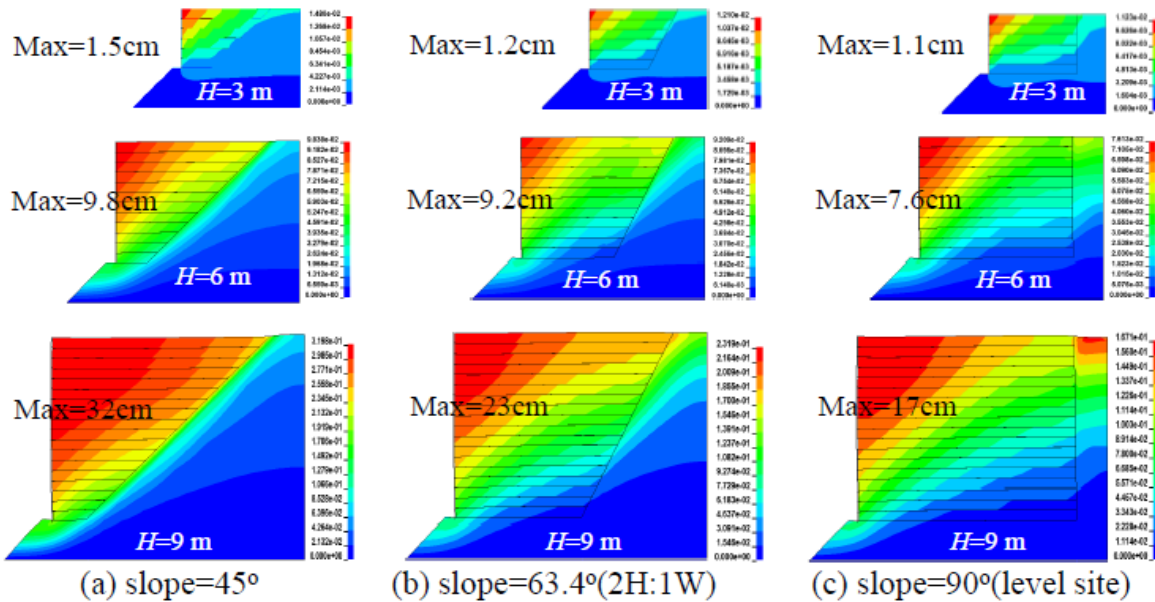
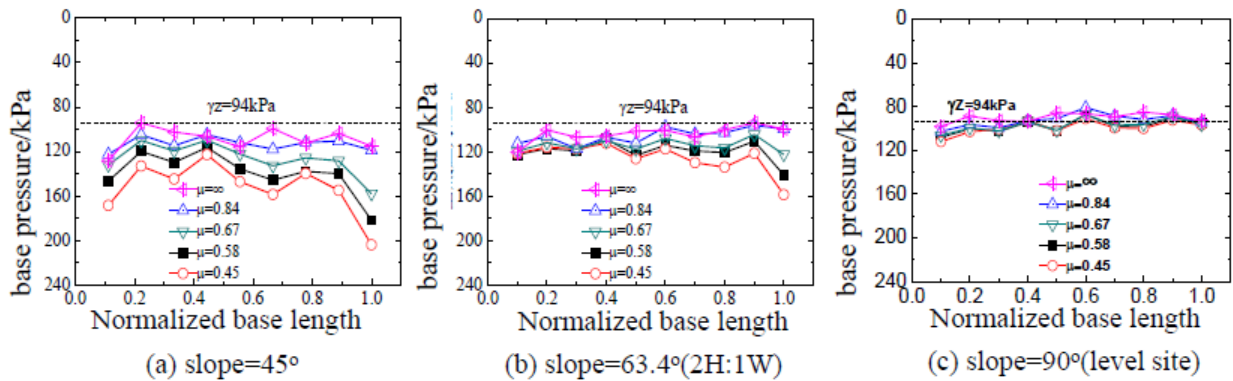
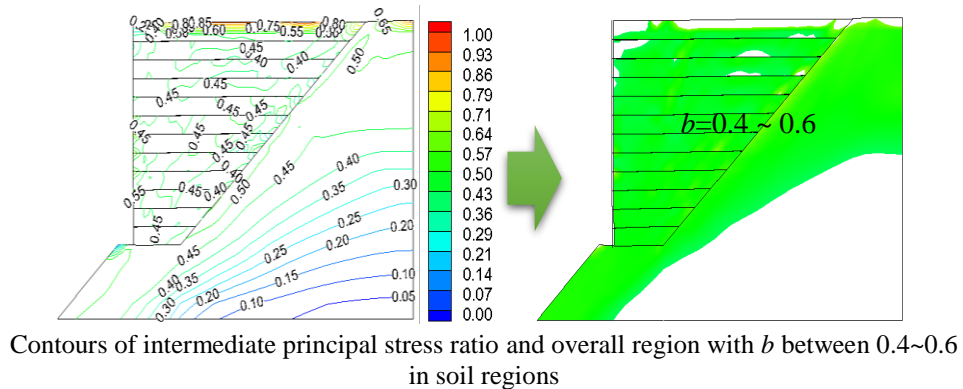


Figure 4.7: Influence of wall height on deformability of GRS walls with 3 different backslopes



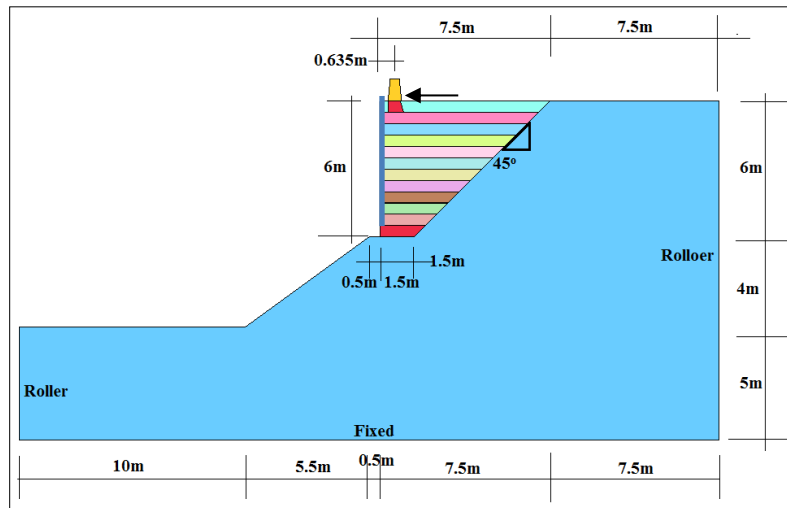
**Figure 4.8: Vertical stress distribution near GRS base under Stage II loading: GRS  $\theta=0.1864$ , foundation  $\theta=0.2143$**



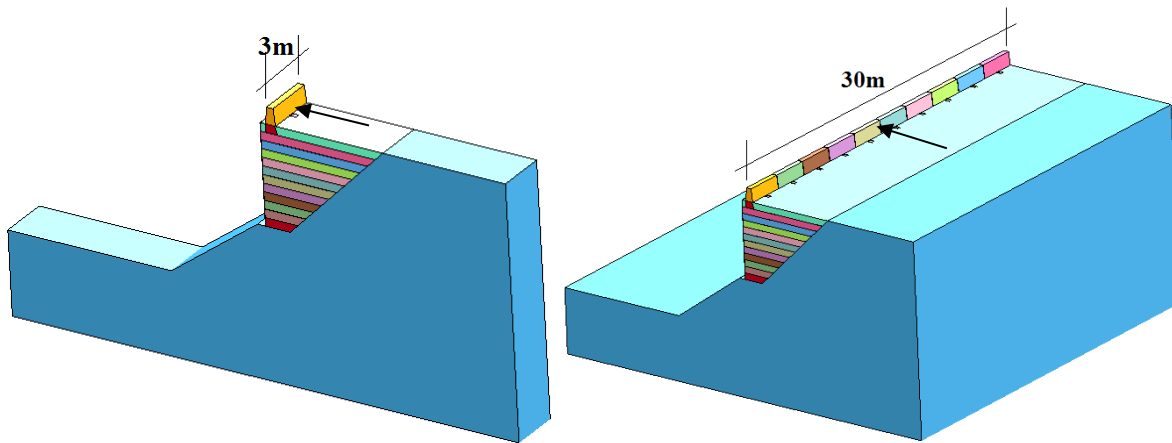
**Figure 4.9: Intermediate principal stress ratio  $b$  in GRS region**

On the basis of the preliminary study and the expected engineering scenarios, it was decided to focus on a nominal 6m-tall hybrid wall configuration with a  $45^\circ$  backslope and discretize the GRS into twelve soil layers and geotextile, as indicated in Fig. 4.10. In the development of the detailed finite element models with refined meshing for resolution, the backfill and slope regions were modeled by 8-node constant stress solid elements for their efficient performance in nonlinear elastoplastic analysis. The 8-node solid element was formulated using one-point integration with viscous hourglass control. The geotextile sheets were taken to be 2mm thick and discretized into 4-node Belytschko-Tsay membrane elements. Belytschko-Tsay membrane element formulation in LS-DYNA was employed for geotextile, as its flexural stiffness is typically negligible (see <http://www.dynasupport.com/tutorial/ls-dyna-users-guide/elements>). The connecting pieces (i.e., dowels and anchors) that are steel bars, were discretized as beam elements. The front concrete

wall panel was modeled by 4-node shell elements with a thickness of 10 cm. The cross section of concrete Jersey barrier was taken to be an isosceles trapezoid with an upper side of 0.4 m, a bottom side of 0.6 m and a height of 1 m. Two adjacent barriers were connected by connecting steel dowels, with 3 cm gaps between them. For a 30m road, ten barriers of 2.97 m in length were lined up and linked.



(a) Nominal dimensions of GRS wall-foundation-barrier-slope domains and boundary conditions (geotextile thickness =2mm, wall facing thickness=20mm)



(b) Single 3m-barrier segment of wall system (c) 30m- multiple barrier segment of wall system

**Figure 4.10: Nominal configuration of truncated GRS wall with back-slope with or without micropiles**

Because of the high number of material components and interfaces in the hybrid GRS-pile-barrier-slope system, the effort in developing the 3D finite element model was significant, requiring

careful design, proportioning, substructuring as well as assembly testing. In the case of the micropiles, different pile sizes were simulated using an equivalent-sectional approach for a common 27cm square cross-sectional geometry to bypass the laborious task of re-meshing for each variation of pile diameters and to ease the difficulty in performance comparison (see Fig. 4.11 for the correspondence between the actual concrete pile size and its equivalent pile Young's modulus used in the finite element model). By the commonly-used material homogenization approach, the mesh thickness of the geotextile was also kept at 2mm and GRS soil layer's at 0.5m to allow the modeling and computational time to be practical.

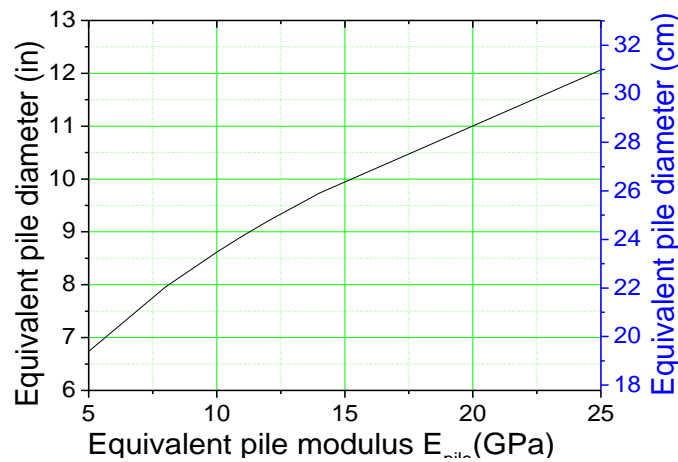


**Figure 4.11: Concrete micropile size in terms of equivalent pile modulus in model**

With the foregoing choices of material parameters and finite elements, different geometric and material configurations for the wall were developed and evaluated to establish a rational basis for comparison, validation and engineering insights. Cases that were considered include truncated walls on slopes with and without micropiles, the modeling of the barriers and grade beams with dowel bar anchorage or connections. Single span models and then multiple span models of micropiles-GRS-barriers were both used, the former for computational efficiency, and the latter for realistic impact modeling where dynamic load transfers to multiple adjacent spans can be expected to occur.

A general layout of a hybrid A-frame Micropile-GRS-barrier-foundation finite element model included the following:

1. A truncated reinforced soil region with layers of soil and geotextiles and a front concrete facing,

2. Pairs of vertical and inclined micropiles in the form of a A-frame structure at regular spacing going through the GRS region to the slope,
3. The concrete micropiles are penetrated into the foundation and backslope to a chosen depth,
4. A concrete road barrier is anchored to a grade beam that, in turn, is connected to the pile caps of the micropiles,
5. Pile cap and grade beam are placed on the pile top to connect the vertical and inclined micropiles and form a longitudinal framing mode along the length of highway so as to increase the integrality of the system.

Details of the finite element modeling of some critical components of the hybrid A-frame micropile- reinforced soil-barrier-on slope are shown in Fig. 4.12 to 4.15.

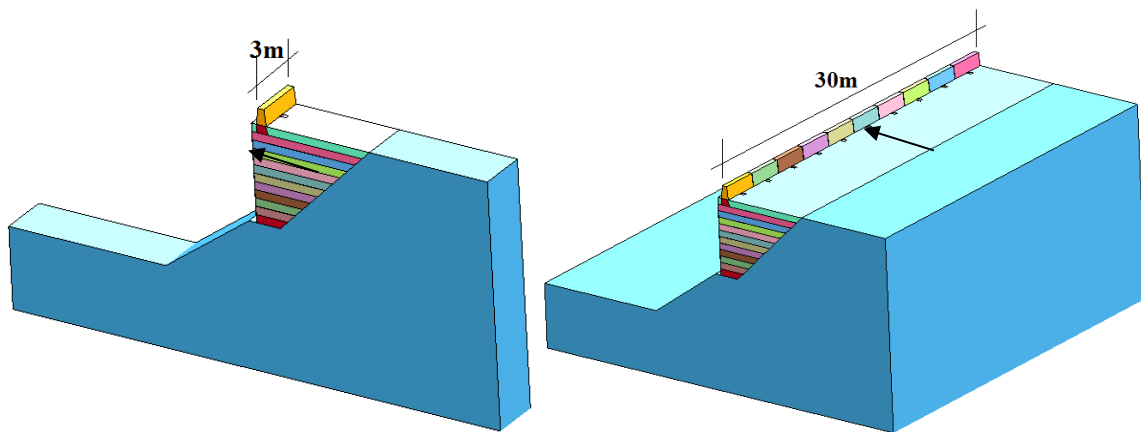


**Figure 4.12: A single 3m-barrier segment and 30m-barrier segment of hybrid wall system**

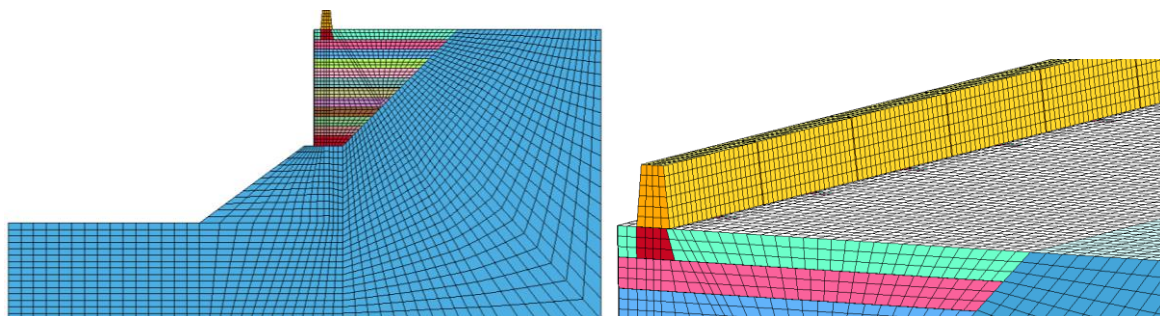


**Figure 4.13: Finite element model for micropile-GRS-barrier-grade beam-anchor-foundation slope system**

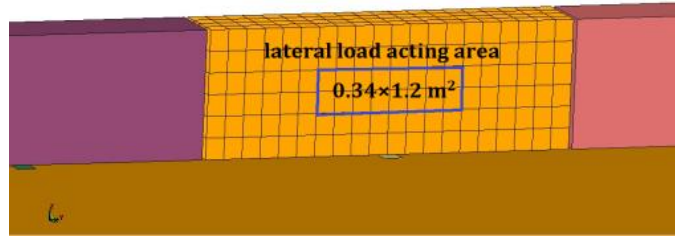


**Figure 4.14: Impact area on finite element barrier model**

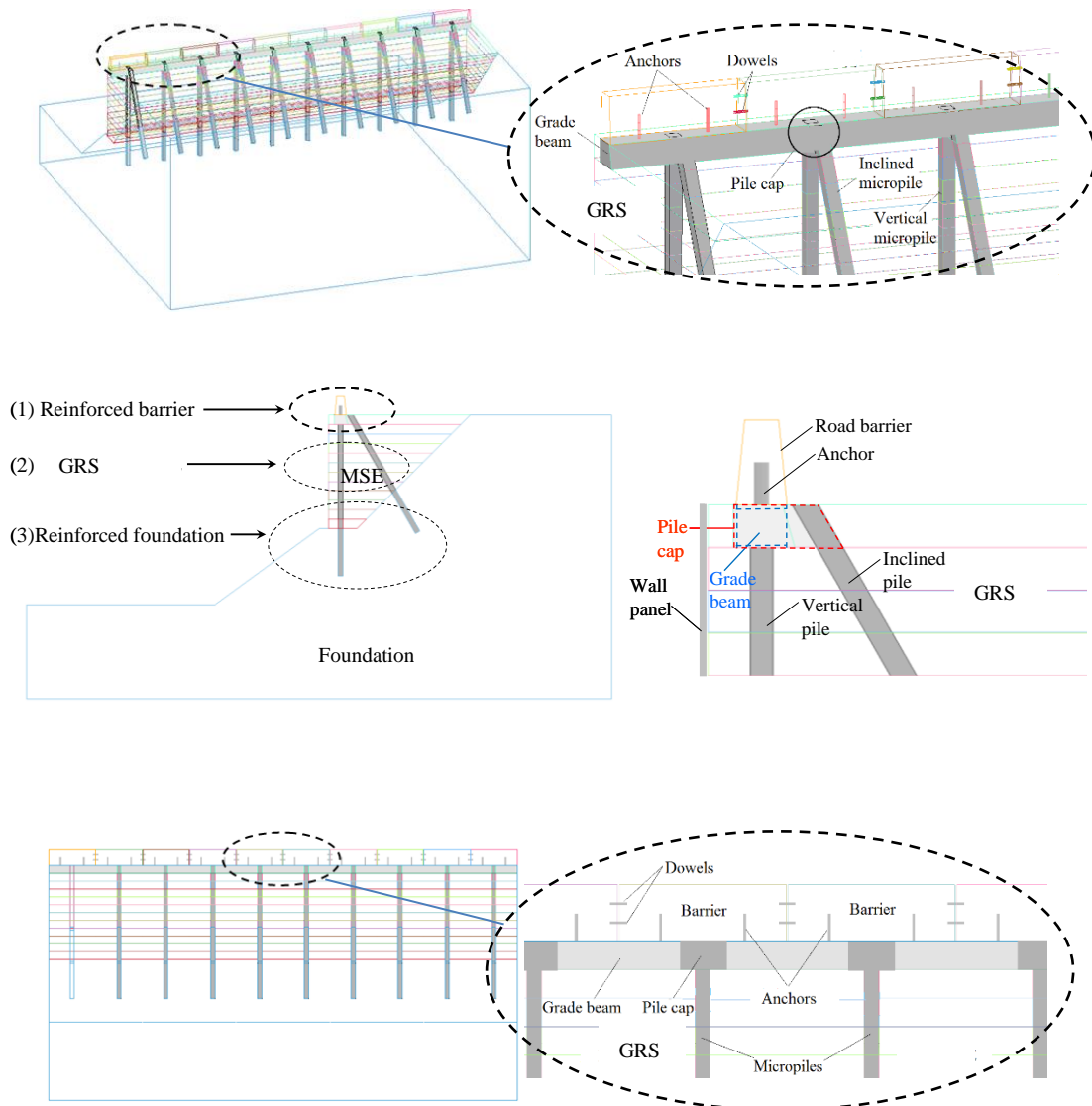


**Figure 4.15: Connection details of finite element model of hybrid micropile A-frame-GRS-grade beam-barrier on slope**

### 4.3 Experimental Confirmation of Finite Element Approach

To gauge the reliability and relevance of the numerical setup and material parameter selection to physical situations, a corresponding laboratory-scale experimental study was conducted by Zhang [18]. The model tests were prepared with a height of 1.5 m, a length of 2 m and a width of 1 m. The dimensions and geometry of GRS walls before and after reinforced with micropiles can be seen in Fig. 4.16. Smooth rigid plastics sheets were used to cover the two inner sides of the test tank to reduce the boundary friction. Three sections of GRS wall models were built and the movement of the middle section was measured and studied. The GRS backfill was a sand and built to 0.6 m tall. It was constructed on a 45° clay foundation, and the thickness of each soil layer was 0.1 m. The total height of the GRS walls was 1.20 m. The cross section of the micropiles was square, with a width of 3 cm. The anchorage depth of the model piles in the foundation was 25 cm, the pile spacing was 1 m, the angle between vertical and inclined micropiles was 30° and the backslope was planar, all intended to be similar to the finite element configuration considered in this project. Cotton cloth with a thickness of 0.2 mm was used as the geotextile and galvanized sheet iron with a thickness of 1 mm was tied to the fabrics and used as the front wall panel. Polymethylmethacrylate piles with square cross sections of 3 cm<sup>2</sup> was used as micropiles. In the tests, surcharge loading was applied by laying bricks uniformly on the top of GRS layer by layer. The surcharge loading per level of bricks was 2 kPa, leading to a final surcharge load of 10 kPa on the backfill. Six dial indicators were placed along the height of wall panel to monitor the lateral displacement of wall panel, and 1 dial indicator was put on the top of bearing plate to record the subsidence of GRS wall. Detailed of the experimental tests can be found in [38].

With the same material models discussed earlier and some minor variations of the material parameters as appropriate (see Table 4.10 and 4.11), LS-DYNA was used to determine the response of the model GRS and the A-frame wall. As can be seen from the comparison shown in Fig. 4.17, the simulation results are in general agreement with the measured wall movements and backfill surface settlement as a function of the loading. While no dynamic impact tests were performed, the agreement in both numbers and trends between the theoretical and experimental results give credence to the physical relevance of the implemented finite element model in handling the multi-component soil-structure interaction problem.

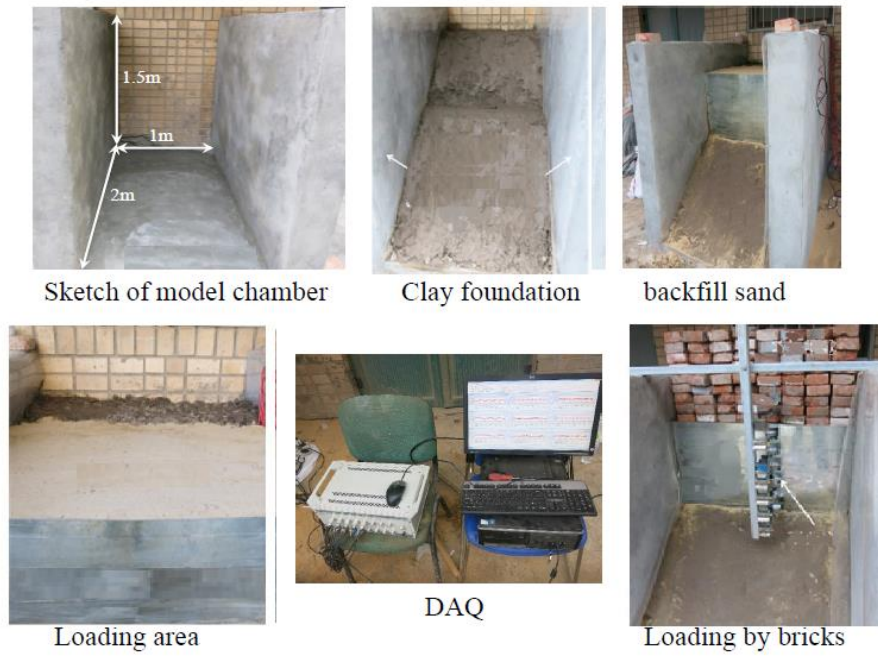


Figure 4.16: Experimental scaled model of GRS wall with and without pile A-frame

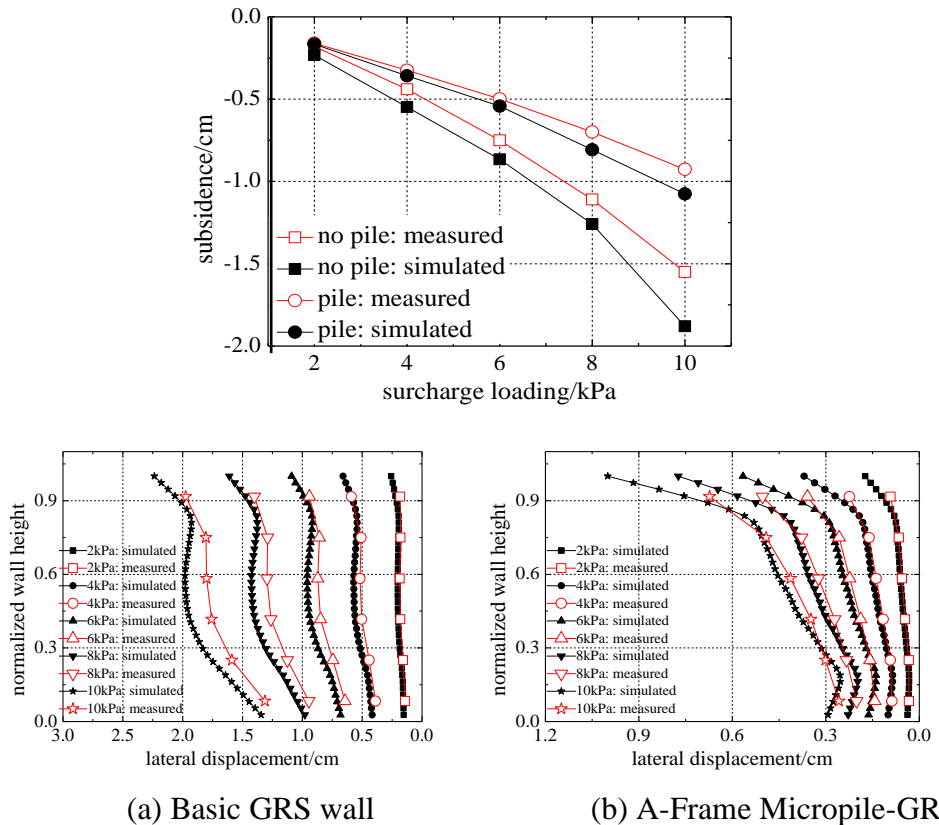


Figure 4.17: Comparison of experimental measurements and finite element model of GRS wall with and without pile A-frame under surcharge

**Table 4.10: Parameters of Geologic Cap Model for experimental soil model [33]**

Parameters	Backfill	Foundation soil
Density (kg/m <sup>3</sup> )	1600	2000
$X_0$ (kPa)	0	0
$G$ (MPa)	10	10
$K$ (MPa)	30	30
$\alpha$ (kPa)	0	22.55 ( $c=24$ kPa)
$\theta$ (radian)	0.1667 ( $\varphi=30^\circ$ )	0.2143 ( $\varphi=20^\circ$ )
$\beta$ (MPa <sup>-1</sup> )	0	0
$\gamma$ (MPa)	0	0
$W$	1	1
$D$ (MPa <sup>-1</sup> )	0.00725	0.00725
$R$	4	4
Tension cutoff (kPa)	0	20

**Table 4.11: Parameters of cloth fabric, wall facing and model micropile [33]**

Parameters Materials	density/(kg/m <sup>3</sup> )	$E$ /(GPa)	Poisson's ratio	$\sigma_y$ /(MPa)	$E_t$ /(MPa)
Geogrid	900	0.254	0.3	31.24	0
Wall panel	7500	210	0.25	-	-
Micropiles	1200	2.9	0.25	-	-

#### 4.4 Static and Dynamic Design Loads

For the evaluation of the response of the hybrid wall system for both serviceability and ultimate limit states, three stages of self- and applied loadings were considered and superimposed in the following order:

**Stage I:** Normal gravity or self-weight load on the GRS,

**Stage II:** Design surface surcharge of 12 kN/m<sup>2</sup> on the backfill of the GRS,

**Stage III:** Dynamic horizontal impact with a peak resultant of 240 kN on the barrier.

Stage I's gravity loading which was turned on slowly in a stepwise manner was to simulate the effect of self-weight so as to set up a realistic initial stress state on which the stress-strain response of the soil depends. Stage II loading was a distributed surface loading that is equivalent to 2 feet of soil) applied to the backfill to represent nominal pavement design loading. Stage III was the FHWA design dynamic impact load of 54 kips (240 kN) that corresponds to a TL-4 impact from vehicles. To realize the desired quasi-static responses for Stage I and II and the dynamic effects in Stage III, their respective loading time histories in the computation shown in Fig. 4.18 were employed. Both single 3m-barrier sections and a continuous 30m section with 3m spacing of the micropiles were considered. The former helped to reduce significantly the computational time that was needed to execute the detailed finite element model and was found to be sufficient for validating Stage I and II's response. The latter was needed to assess realistically the three-dimensional response and sideway load transfers in the connected multi-barrier-piles-GRS system during Stage III loading, i.e., the impact scenario.

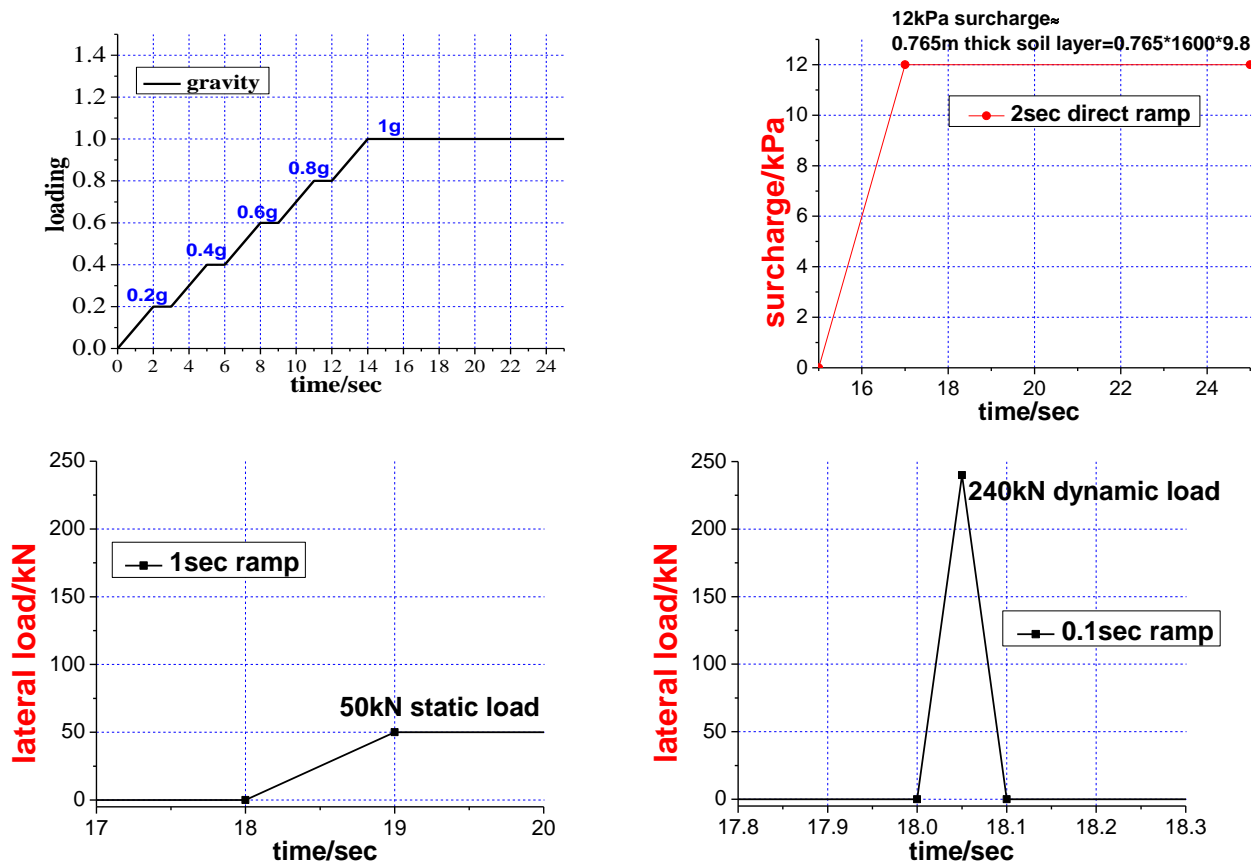


Figure 4.18: Load-time sequences used in Loading Stages I, II and III

## **5 PERFORMANCE ASSESSMENT OF HYBRID MICROPILE A-FRAME-GRS-BARRIER DESIGN**

With the presence of multiple material components of the hybrid wall such as the soil, the micropiles, the geotextile and others, both the global and local conditions of the system's components under loading were examined:

### **5.1 Overall Deformation of Hybrid Wall in 3 Load Stages**

By means of LS-DYNA, the displacement responses of a basic truncated GRS wall with no pile reinforcement versus one with micropile A-frames that are spaced at 3m using both a representative 3m-wide segment versus a 30m-wide wall were computed sequentially for Stage I to Stage III loading. From Stage I's and Stage II's results that are shown in Fig. 5.1 to 5.4 and Fig. 5.5 to 5.8, respectively, one can see that the 3m wall and 30m wall sections under gravity and surcharge loadings, yield similar results. This is expected because of the span-wise regularity of the GRS-pile-barrier system in the longitudinal wall direction, with the minor variation being a consequence of the difference in the distance of the central section from the end's. A much larger difference in the deformation response can be observed between the truncated wall with no micropile and one with micropiles under Stage III impact loading as shown in Fig. 5.9 to 5.12. Specifically, the 30m micropile A-frame-GRS- system has its maximum barrier displacement increased by 0.42cm beyond Stage II's response due to the impact, while the basic 30m truncated GRS section whose concrete barriers are anchored directly to the GRS incurred a movement of 6cm, i.e. 14 times more. The substantial difference in response between a 3m- and a 30m-wall segment in Stage III loading is mainly due to the use of the plane-strain roller-type/frictionless boundaries on the 2 vertical sides of the 3m section which nullifies much of the resistance that the adjacent segments of the hybrid wall system would otherwise provide to resist the impact loading. For more insights, a comparison of the amount and type of barrier movement in the case of a basic GRS versus a hybrid micropile-GRS under a high impact force of 600kN is shown in Fig. 5.13.

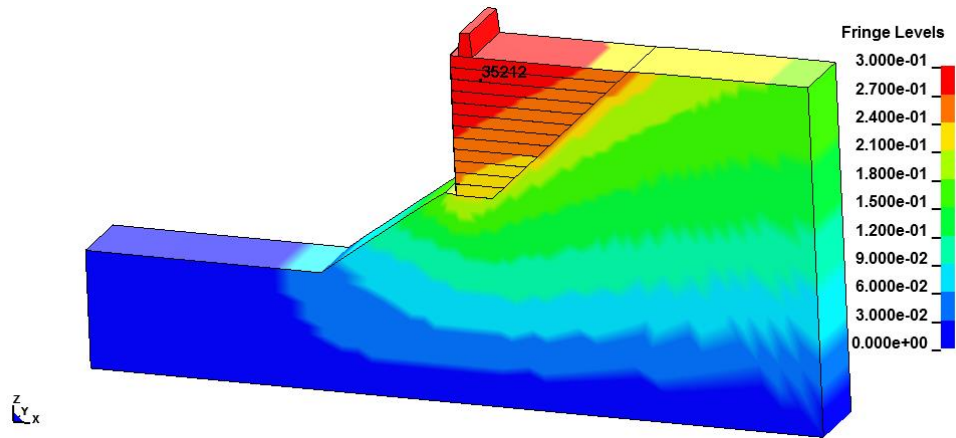


**Figure 5.1: Resultant displacement of 3m truncated basic GRS in Stage I-gravity: max=29.2 cm near anchor tip: foundation  $\theta_{nominal}=0.2143$**

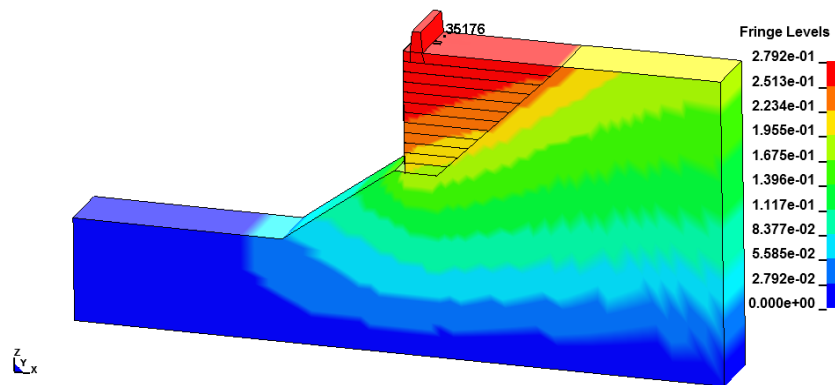


**Figure 5.2: Resultant displacement of 3m GRS-pile model in Stage I-gravity: max=27.9 cm near barrier base:  $\theta_{nominal}=0.2143$ ,  $E_{pile}=12\text{GPa}$  (9" pile)**

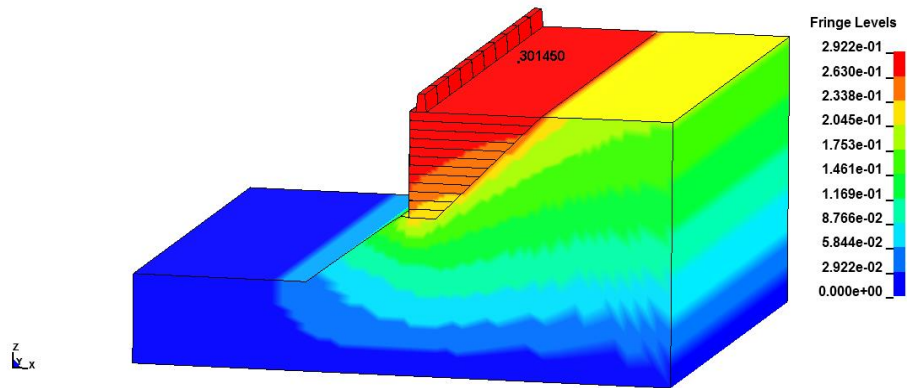


**Figure 5.3: Resultant displacement of 30m truncated basic GRS under gravity: max=29.2 cm near anchor tip: foundation  $\theta_{nominal} = 0.2143$**

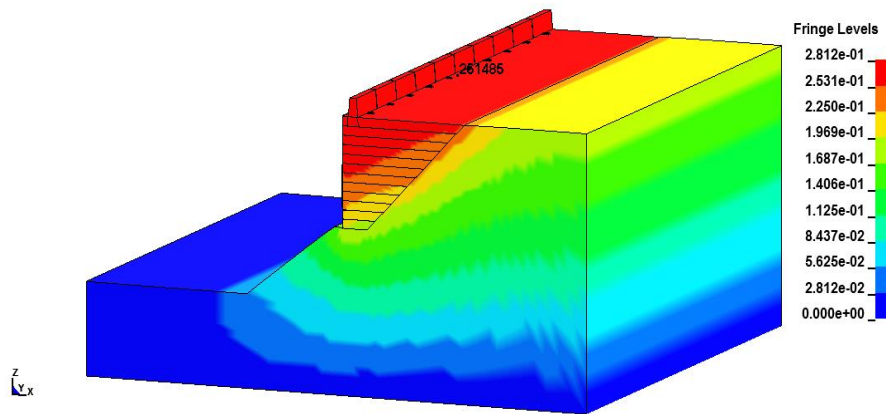


**Figure 5.4: Resultant displacement of 30m GRS-pile model under gravity: max=28.1 cm near barrier: foundation  $\theta_{nominal} = 0.2143$ ,  $E_{pile} = 12\text{GPa}$  (9" pile)**

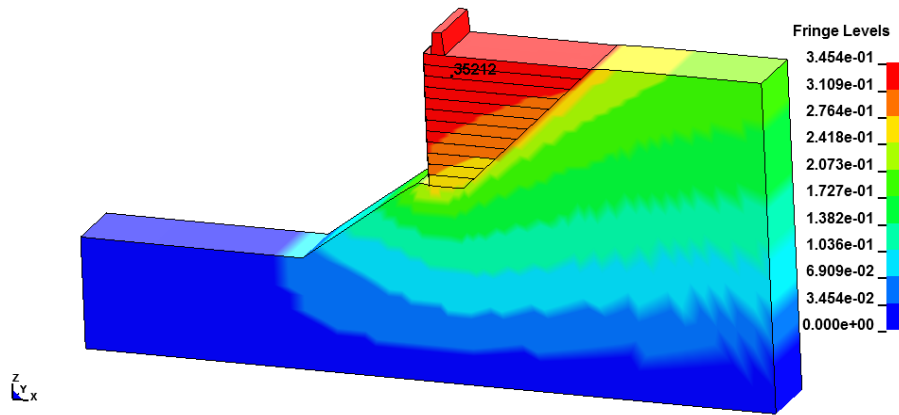


**Figure 5.5: Cumulative resultant displacement of 3m- truncated basic GRS in Stage II-surcharge: max=34.5 cm at anchor tip: foundation  $\theta_{nominal} = 0.2143$**

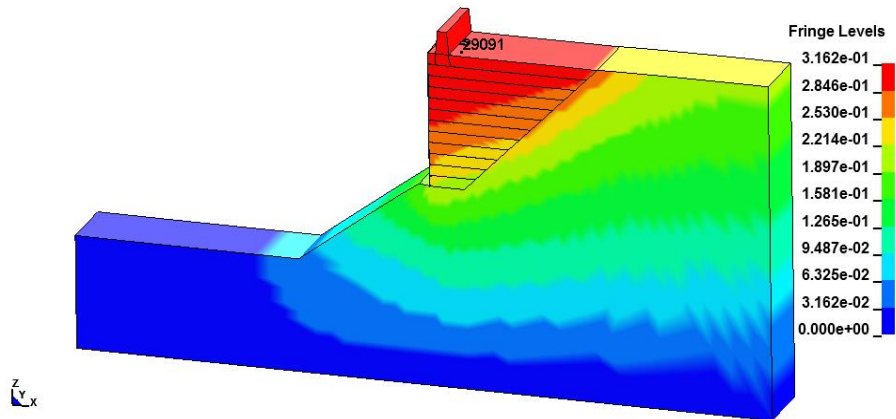


**Figure 5.6: Cumulative resultant displacement of 3m GRS-pile in Stage II-surcharge: max=31.6 cm near barrier: foundation  $\theta_{nominal}=0.2143$ ,  $E_{pile}=12\text{GPa}$  (9" pile)**

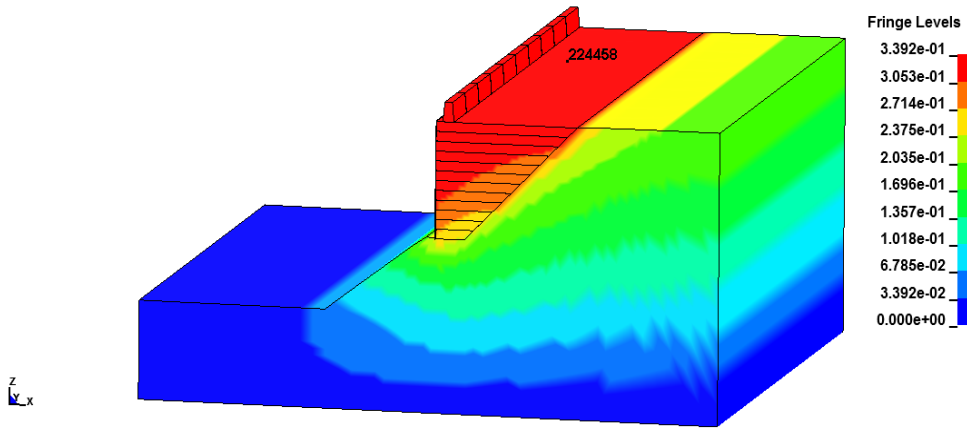


**Figure 5.7: Cumulative resultant displacement of 30m- truncated basic GRS in Stage II-surge: max=33.9 cm at anchor tip: foundation  $\theta_{nominal}=0.2143$ .**

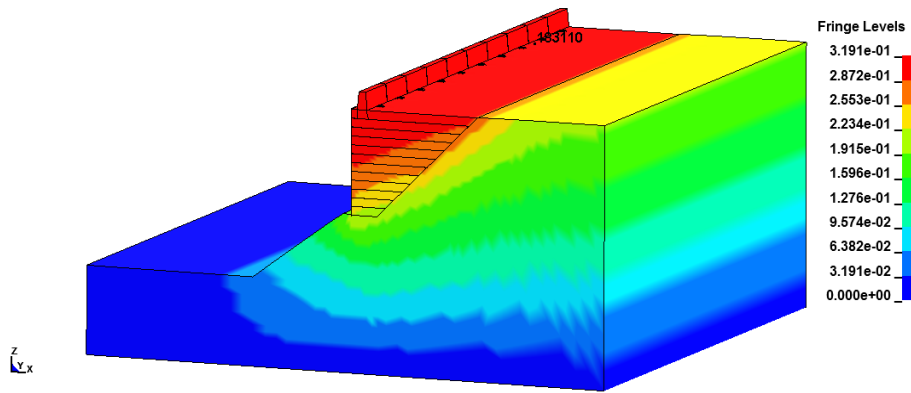


**Figure 5.8: Cumulative resultant displacement of 30m-GRS-pile in Stage II-surge: max=31.91 cm near barrier: foundation  $\theta_{nominal}=0.2143$   $E_{pile}=12\text{GPa}$  (9”pile)**

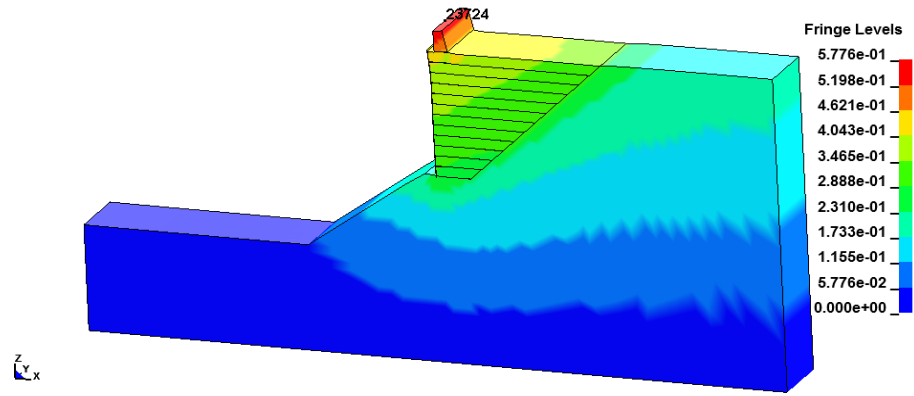


**Figure 5.9: Cumulative resultant displacement of 3m truncated basic GRS in Stage III-dynamic impact, max>57.7 cm at barrier top: foundation  $\theta_{nominal} = 0.2143$**

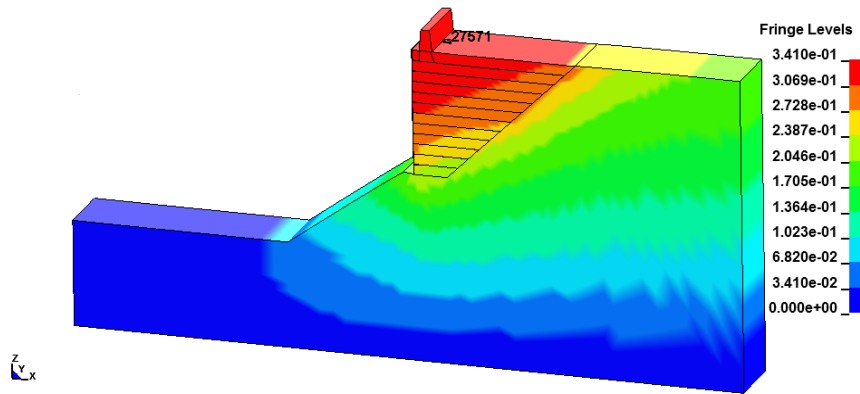


**Figure 5.10: Cumulative resultant displacement of 3m GRS-pile in Stage III-dynamic, max=34.1 cm near barrier: foundation  $\theta_{nominal} = 0.2143$ .  $E_{pile} = 12\text{GPa}$  (9" pile)**

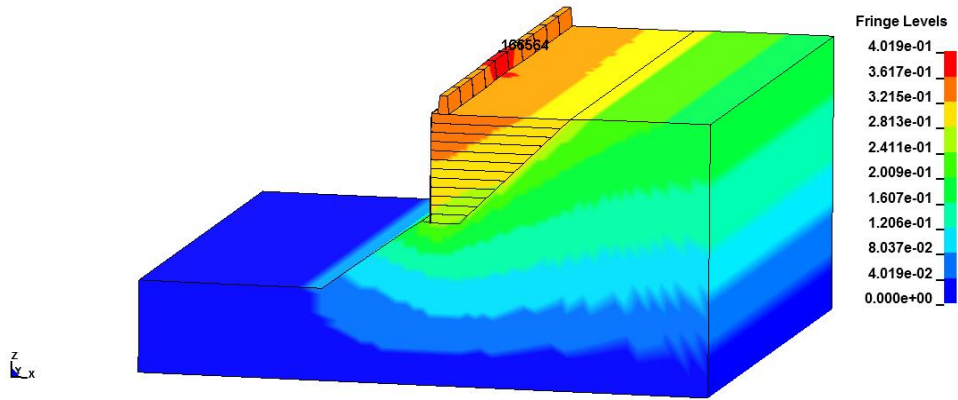


**Figure 5.11: Cumulative resultant displacement of 30m truncated basic GRS in Stage III-dynamic, max=40.2 cm at barrier top: foundation  $\theta_{nominal} = 0.2143$**

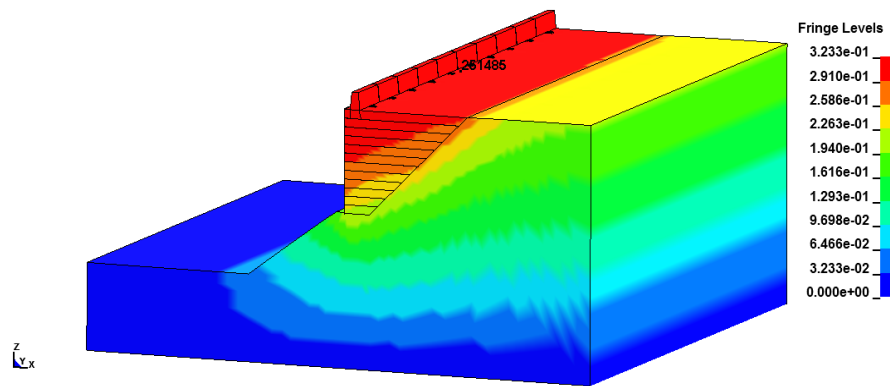
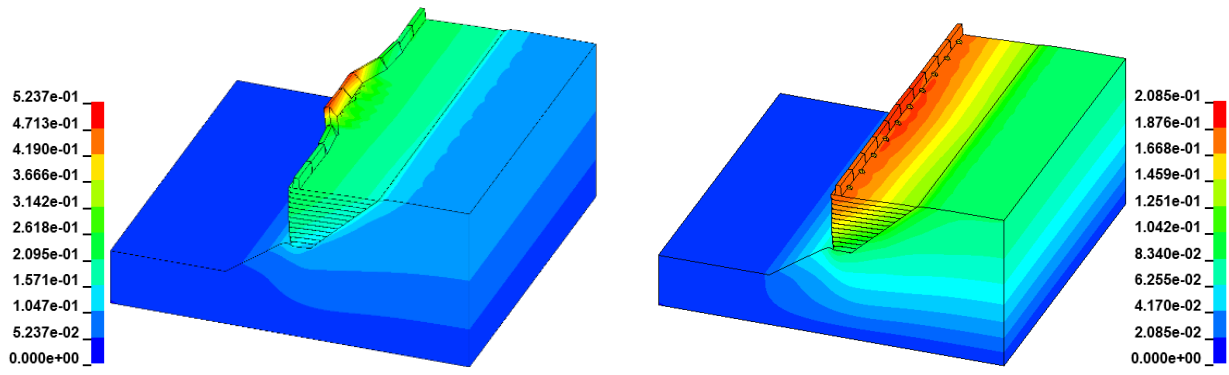


**Figure 5.12: Cumulative resultant displacement of 30m GRS-pile in Stage III-dynamic, max=32.3 cm near barrier:  $\theta_{nominal} = 0.2143$ .  $E_{pile} = 12\text{GPa}$  (9" pile)**



(a) Deformation of basic GRS wall                      (b) Deformation of hybrid micropile/GRS Wall

**Figure 5.13: Accumulated resultant displacements (magnified by 5 times) at  $t=0.20$  sec under front impact of 600 kN peak load**

## 5.2 Lateral Earth Pressure in Basic GRS versus GRS-Micropile System

For retaining wall design, the classical Rankine earth pressure theory (see Fig. 5.14) has been a common reference. It describes the limit state of active earth pressure in terms of the active earth pressure coefficient of

$$K_a = \tan^2(45^\circ - \varphi/2)$$

which gives 0.283 for a GRS's soil's internal angle of friction  $\varphi = 34^\circ$  for example. For at-rest conditions, Jaky's formula of  $K_0 = 1 - \sin\varphi$  gives 0.441 for the same friction angle.

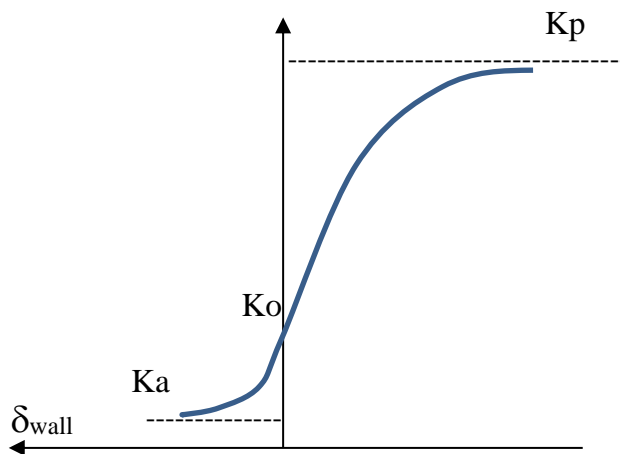


**Figure 5.14: Active, passive and at-rest earth pressure coefficients**

Illustrated in Fig. 5.15 and 5.16 are the LS-DYNA results for the lateral soil pressure in the GRS with and without the micropiles. As a useful reference, the truncated GRS wall without micropiles is first considered. Relative to the classical Rankine active pressure theory, one can see that the lateral earth pressure in the backfill is higher at the top, lower at the middle and higher at the bottom. This reflects the effects of the weight of barrier at the top, strengthening of the soil by the geotextile reinforcements and the influence of the bottom boundary conditions, respectively. Due to the impact load in Stage III, one can observe that there is a sizable increase in the lateral stress in the soil's top region. This correlates well to the large displacement response of the barrier found for the case as discussed earlier. With the A-frame micropile-GRS design, however, the lateral pressure situation is significantly mitigated. While there is a notable increase in residual lateral pressure in the basic GRS wall after impact, the increase is much less in a GRS-micropile wall system.

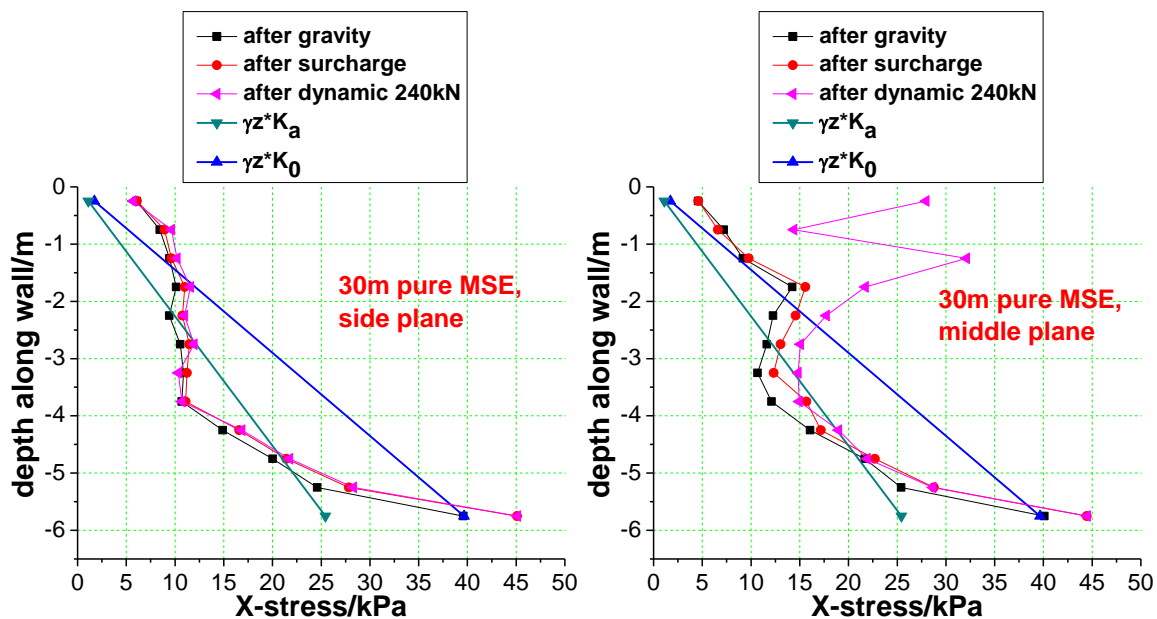


**Figure 5.15: Horizontal normal soil stress next to wall facing for 30m truncated GRS at side and mid-sections (GRS  $\theta=0.1864$ , foundation  $\theta=0.2143$ )**

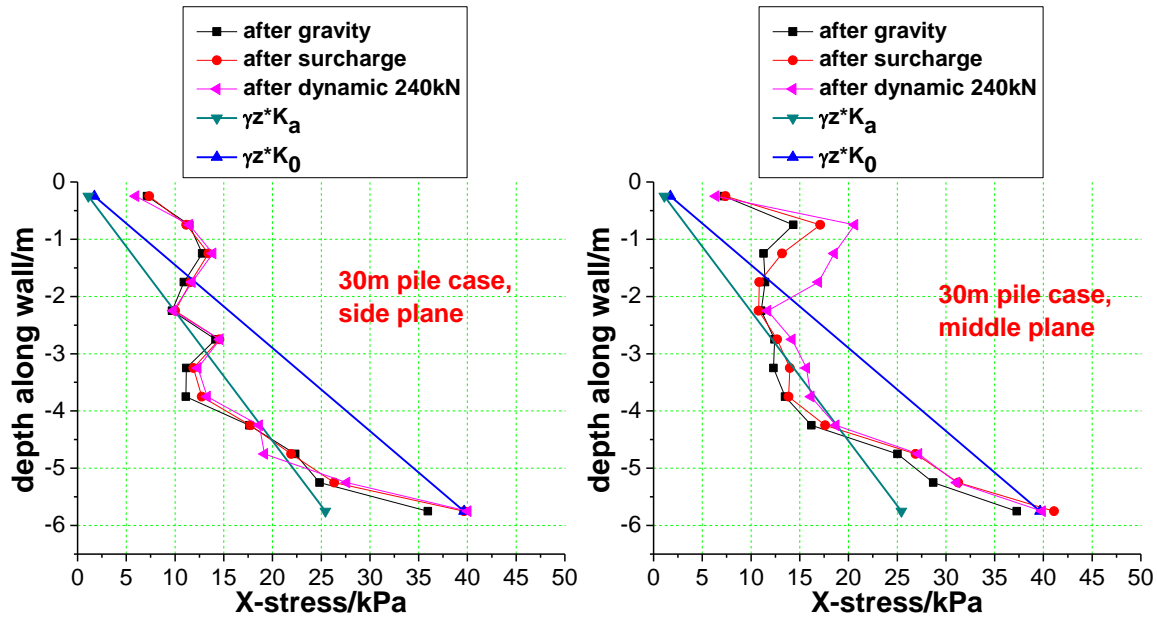
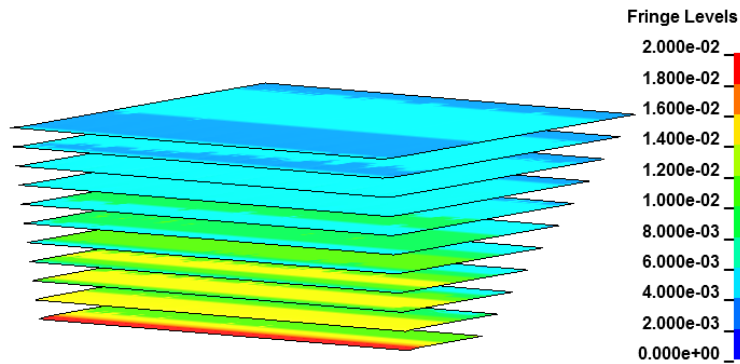


Figure 5.16: Horizontal normal soil stress next to wall facing for 30 GRS–pile case (GRS  $\theta=0.1864$ , foundation  $\theta=0.2143$ , 9” pile ( $E_{pile}=12\text{GPa}$ ))

### 5.3 Geotextile Responses in 30m GRS and 30m GRS-Micropile Wall with 9” micropiles

Fig. 5.17-5.22 show the spatial variation of the strain in the geotextile in the GRS with and without 9” micropiles (12 GPa equivalent pile modulus) under Stage I, II and III loading with the nominal soil condition of  $\theta=0.1864$  ( $\varphi=34^\circ$  at  $b=0.5$ ) in the GRS region and  $\theta=0.2143$  ( $\varphi=40^\circ$  at  $b=0.5$ ) in the foundation region. As can be seen in the first two figures for gravity loading or self-weight, there is no significant difference in the geotextile response between the 30m basic GRS and the 30m micropile-GRS cases.



**Figure 5.17: Geotextile  $\epsilon_x$  strain of 30m truncated basic GRS in Stage I-gravity (GRS  $\theta=0.1864$ , foundation  $\theta=0.2143$ , max=2.75% at bottom)**

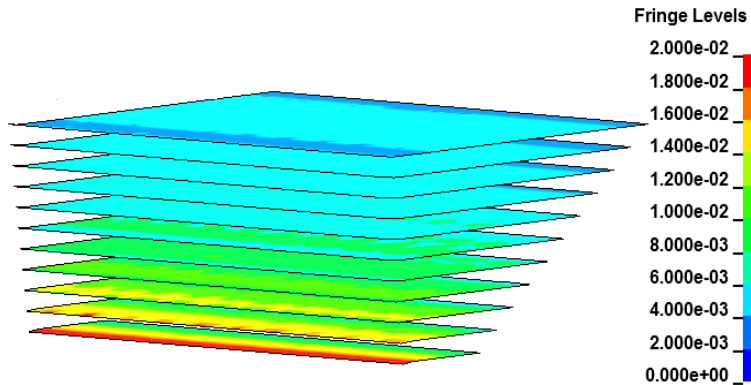


**Figure 5.18: Geotextile  $\epsilon_x$  strain in 30m GRS with piles,  $E_{pile}=12\text{GPa}$  (9" pile) in Stage I-gravity (GRS  $\theta=0.1864$ , foundation  $\theta=0.2143$ , max=3.08% at bottom membrane edge)**

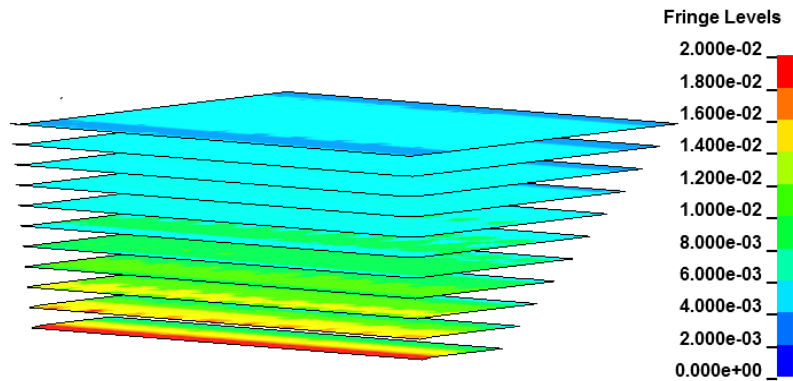


**Figure 5.19: Geotextile  $\epsilon_x$  strain of 30m truncated basic GRS in Stage II-surcharge (GRS  $\theta=0.1864$ , foundation  $\theta=0.2143$ , scale=2%), max=3.32% at bottom membrane edge, top fabric strain=0.4%**

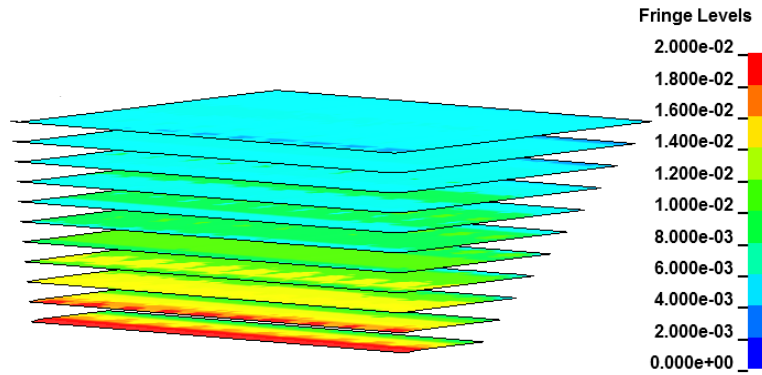


**Figure 5.20: Geotextile  $\epsilon_x$  strain of 30m wall with piles,  $E_{pile}=12\text{GPa}$  (9" pile) in Stage II-surcharge (GRS  $\theta=0.1864$ , foundation  $\theta=0.2143$ , scale=2%) max=3.54% at bottom membrane edge, top fabric strain=0.3%**

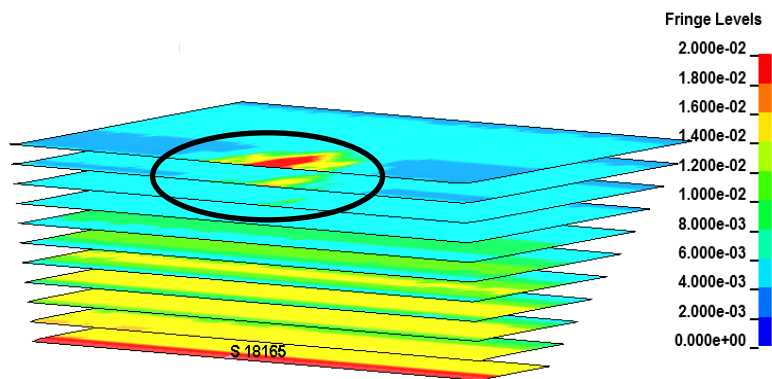


**Figure 5.21: Geotextile  $\epsilon_x$  strain of 30m truncated basic GRS in Stage III-dynamic impact (GRS  $\theta=0.1864$ , foundation  $\theta=0.2143$ ) max=3.4% at bottom membrane edge, top fabric strain=2%**

Under Stage II loading, results in Fig. 5.21 and 5.22 indicate that the geotextile strain in the GRS-only and GRS-pile systems in Stage II –surcharge become slightly higher than those in Stage I, as expected.

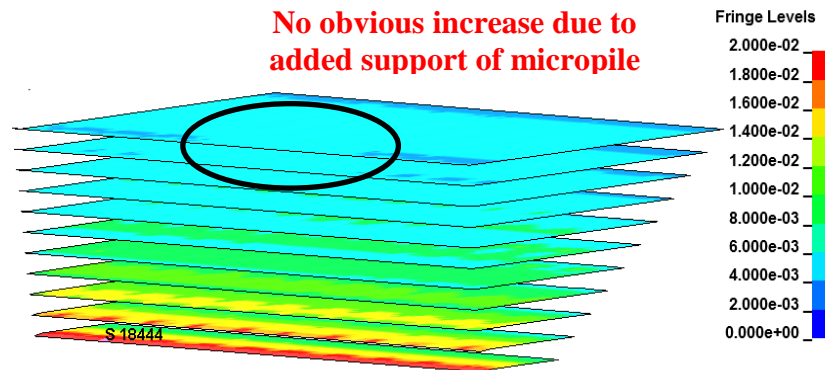


**Figure 5.22: Geotextile  $\epsilon_x$  strain of 30m wall with piles,  $E=12\text{GPa}$  (9" pile) in Stage III- impact (MSE  $\theta=0.1864$ , foundation  $\theta=0.2143$ ) max=3.6% at bottom membrane edge, top fabric strain=0.6%**

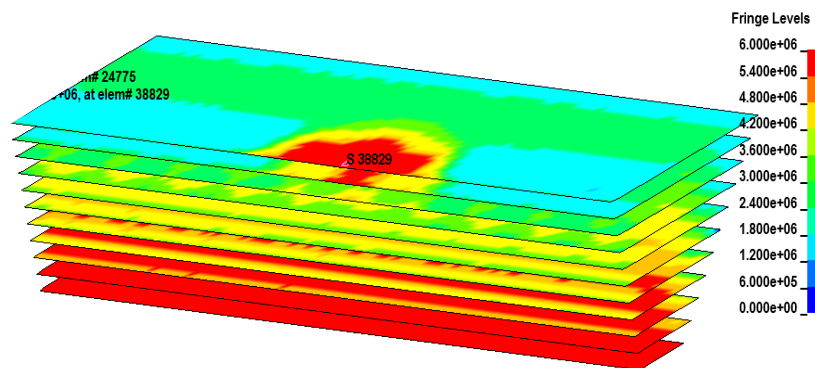


**Figure 5.23: Geotextile  $\sigma_x$  stress in 30m truncated basic GRS in Phase III- dynamic impact on barrier: (MSE  $\theta=0.1864$ , foundation  $\theta=0.2143$ )**

Under Stage III-barrier impact loading, the computed geotextile's strain beneath the barrier down to about 1.5m is much higher in a basic GRS (without the cover of any concrete pavement or moment slab) than the one stiffened by a micropile A-frame system as shown in Fig. 5.23 and 5.24. The localized deformation in the former is likely the result of the concentrated load-transfer from the barrier to the GRS through only the barrier's base contact and regular anchor posts in the

model. In current CDOT practice, such a problem is avoided by anchoring the barriers to an 8' (2.4 m) wide moment slab which helps to spread the load more evenly to the GRS. As illustrated in this study, the added stiffness of the micropile A-frame to the hybrid wall design can provide comparable relief in the load transfer to the GRS from road barriers under TL-4 impact loading.

#### 5.4 Base Pressure under Truncated GRS

With the truncated GRS geometry, the level of reduction in the margin of safety against the bearing capacity of the foundation is a logical concern. By LS-DYNA, the bearing pressure distribution at the narrow base of the 6m GRS wall with a 45° backslope in Fig. 4.5a were computed for different interfacial-friction conditions and the results are shown in Fig. 5.24a and b. With the ideal bonded condition between the GRS and the back slope, one can see that the bearing pressure is a modest 15% higher than that of the regular level-ground condition. Should the coefficient of friction be less, e.g., to  $\frac{2}{3} \cdot \tan(34^\circ)$  or 0.45, however, one can see from the simulation that the soil bearing pressure can potentially double at the inner corner for a 45° backslope. This illustrates that the detailed soil-to-soil interfacial condition at the backslope is important as it can affect significantly the bearing pressure imposed on the foundation by the truncated GRS configuration. With the micropile A-frame, on the other hand, the soil bearing stress is far less sensitive to the exact backslope condition as can be seen from Fig.5.24b and points to another favorable feature of the hybrid micropile-GRS design.

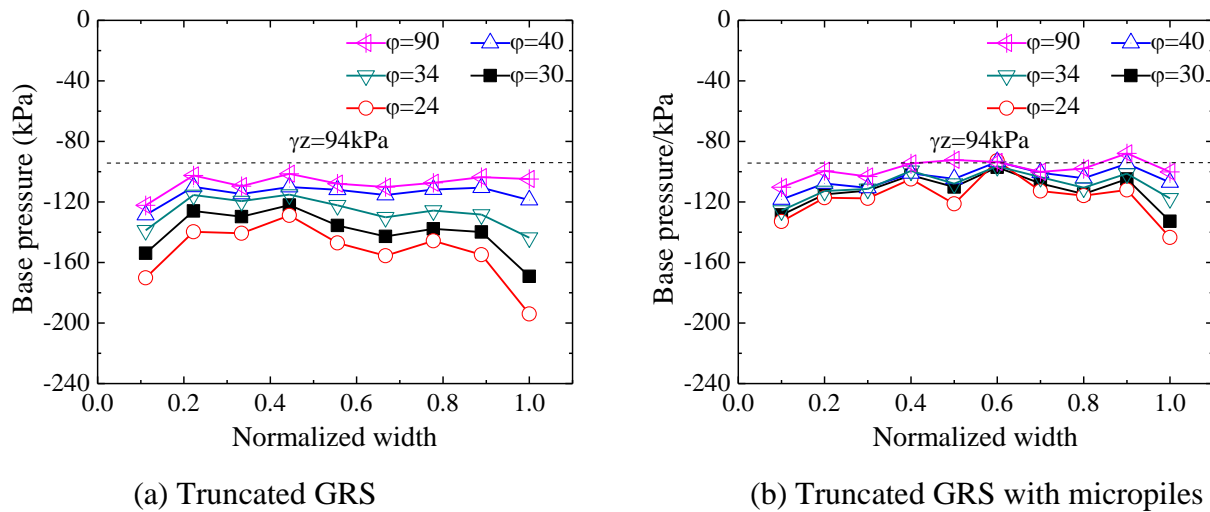


**Figure 5.24: Comparison of truncated soil bearing pressure with different interfacial friction angles under gravity load**

## 5.5 Bending Moment in Micropiles

Checking on the response of the micropiles, Fig. 5.25 shows the bending moment of the vertical and inclined piles in the micropile-GRS wall with different interfacial friction coefficient  $\mu$  between the GRS and the slope in Stage II loading. One can see that the bending moment in the pile would increase as the interfacial friction coefficient decreases. This is consistent with the expectation that micropiles would be asked to support a higher load due to the increase in tendency for the GRS to slide. The bending moment of the vertical micropile reverses from positive to negative with an inflection point at about 1m below the bench for the base consistently. For the inclined pile, the inflexion point is about 0.5m into the slope but goes deeper as  $\mu$  gets smaller. One can also note from Figure 5.25 that the maximum bending moment of the inclined micropile increases more rapidly than the vertical pile's as the interfacial friction coefficient reduces, indicating that the inclined micropile acts in an anti-sliding mode in such circumstances. These insights should be pertinent in configuring the detailed layout of the micropile-GRS design.

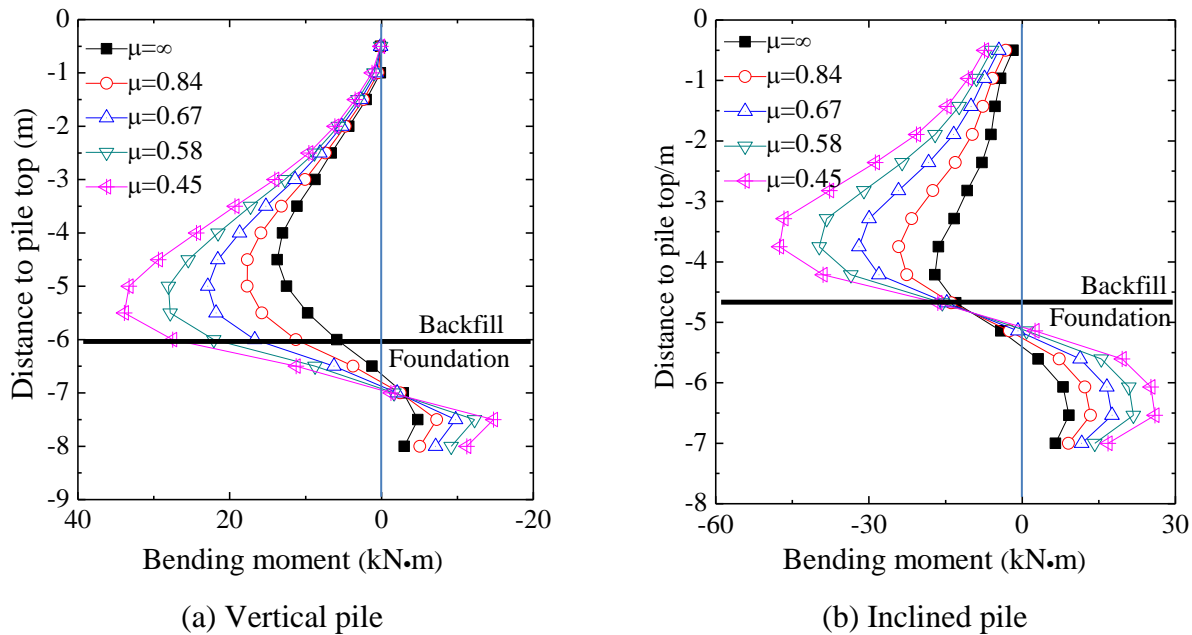


**Figure 5.25: Bending moment of piles in the micropile-GRS wall with different interfacial friction coefficients under gravity and surcharge**

## 5.6 Lateral Movement of Barrier under Impact

To provide more complete information for design, different micropile sizes were studied in regard to both their peak and residual response due to impact loading. Representative result of the

displacement variation with time is shown in Fig. 5.26 for a 9” micropile in Stage III. With the GRS-micropile design, one can see that the residual barrier movement is reduced to 0.5cm from 11.5cm in the case of a basic GRS construction without a moment slab (see Fig. 5.26). Plotted in Fig. 5.27 is the relation between the magnitude of the barrier movement caused by impact as a function of the pile size or stiffness for a 3m-segment of the GRS-pile system, 2 different anchorage depths and a 30m-GRS-pile wall with 2.5m of anchorage. Focused on the 30m case which is the most relevant to the single 240kN impact problem, one can see that the use of micropiles of 8” diameter (equivalent to  $E_{pile}= 8\text{GPa}$ ) or bigger at 3m (9 ft.) spacing and 2.5m (8 ft.) anchorage will give a barrier displacement of 0.7cm (i.e., 0.3 inch) or smaller. This is about 10% of the movement of the barrier when it is directly anchored into a basic GRS.

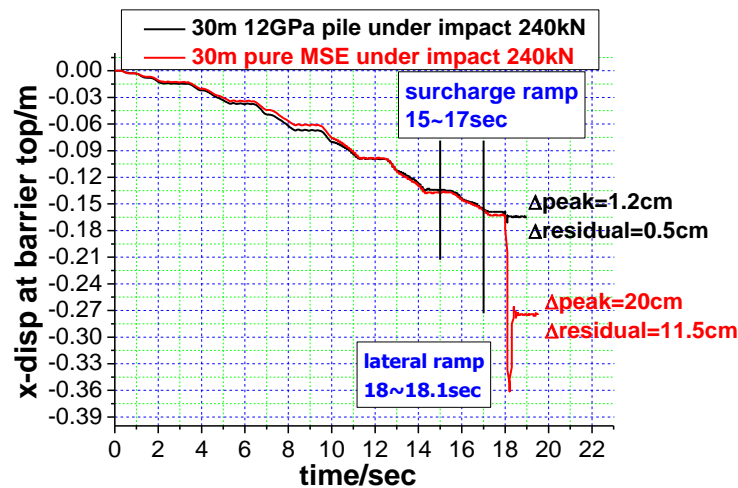


**Figure 5.26: Horizontal barrier response of 30m MSE-12GPa, pile versus pure GRS under dynamic 240kN impact load**

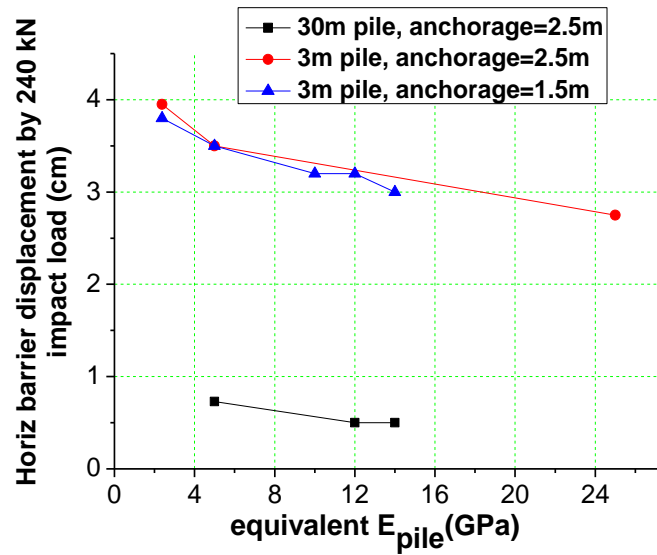


**Figure 5.27: Effect of pile size on barrier movement upon impact in a GRS-pile system (foundation  $\theta=0.2143$ )**

To evaluate the margin of safety in the sense of load-factor design as well as to account for the possibility of higher vehicle speed in down-sloping mountain highway, the response to 5 different impact force levels up to 600 kN, equivalent to applying a load-factor of up to 2.5, was also considered (see Fig. 5.28). They correspond to 21.6 km/hr, 43.2 km/hr, 64.8 km/hr, 86.4 km/hr and 108 km/hr, with an impulse time of 0.10 sec [24] and impact angles of  $90^\circ$  (front impact) and  $20^\circ$  (oblique impact) from the plane of the barrier were considered (see Fig. 5.29), with the centroid of vehicular impact area of  $0.34 \times 0.6 \text{ m}^2$  taken to be at the connection point between two barriers, the likely weakest point. Instead of using the lower bound of soil strength  $\phi=34^\circ$  for the backfill as in earlier simulations, the higher friction angle of  $\phi=40^\circ$  was assumed for the soil in the GRS for more favorable performance from a basic truncated GRS.

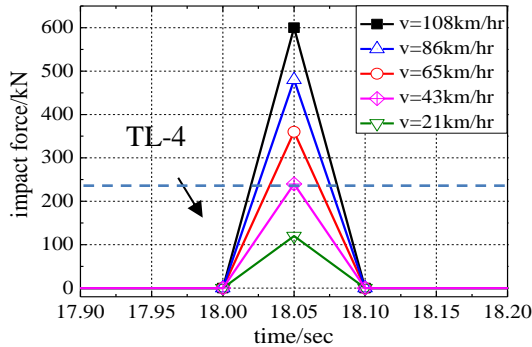


**Figure 5.28: Multiple impact load time histories on barrier**

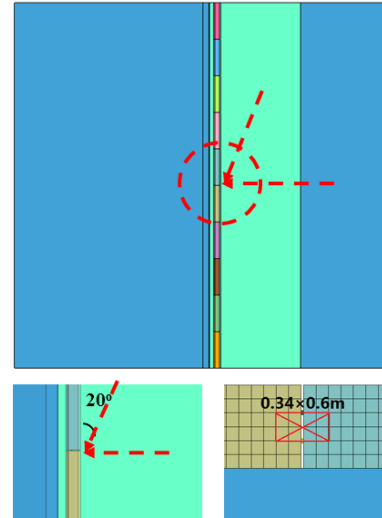


**Figure 5.29: Normal and oblique impact on barrier**

A summary of the peak and residual lateral displacements of barrier under TL-4 (240 kN) and 4 other impact levels, is given in Fig. 5.30 where the “pile” in the legend stands for “hybrid A-frame micropile-GRS Wall” case, while “no pile” stands for the “basic GRS wall” case. From the results, one may note the following:

- Under frontal impact at the TL-4 level, the simulated peak lateral displacement of the barrier anchored to a basic GRS wall is 26.5 cm (10”), and the residual displacement is 16 cm (6.3”). In contrast, the peak lateral barrier displacement of hybrid A-Frame micropile-GRS wall is 2 cm (0.79”) and the residual displacement is 1.2 cm (0.47”), indicative of the ability of the hybrid design to handle impact.
- Under the 20°-oblique impact loading at the TL-4 level (see Fig. 43(b)), the peak lateral barrier displacement of a basic GRS wall is about 12.7 cm (5”) and the residual is 8 cm (3.1”). In contrast, the peak barrier base displacement of the hybrid A-frame GRS wall is 1 cm (0.4”) and the residual displacement is 0.6 cm (0.24”), showing the same stiffening effects. Under 20° oblique impact loading, the lateral deflection profile of the barrier exhibits similar trend but loses the symmetry with respect to the central plane due to the transverse force component.

Generally, the use of the micropile-GRS design is found to lead to a reduction of the barrier movement under impact of the order of 90%, demonstrating the increased stiffness of the proposed system. The stronger structural-foundation configuration allows the impact loading on the barrier

to be transferred in a distributed manner from the barrier to the micropiles and then onto the GRS and the foundation. It provides a potential alternative to continuous or jointed moment slabs for supporting road barriers ([6] and [7]) under TL-4 impact. By designing the micropiles to penetrate more deeply into the foundation region, the hybrid design offers the option to add to the local stability of the slope, as will be illustrated later.

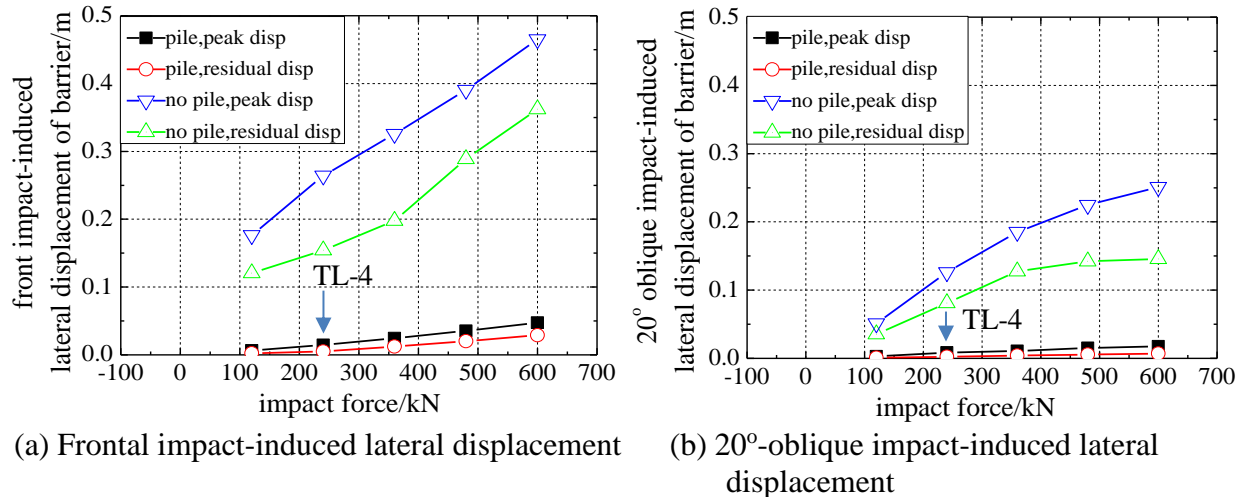
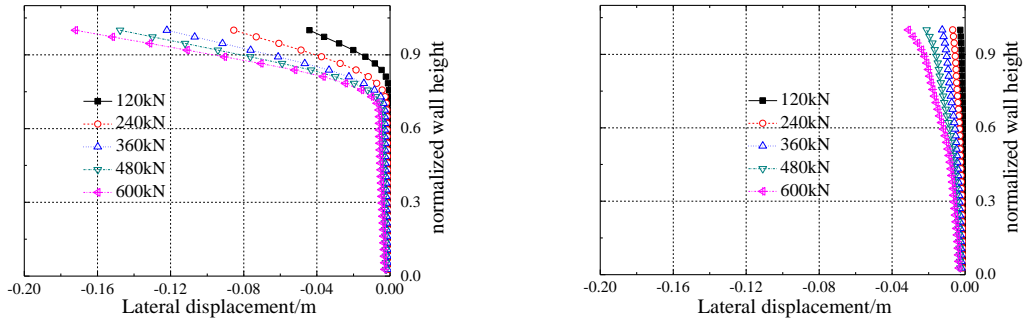


**Figure 5.30: Comparison of barrier lateral displacement induced by different impact load levels**

### 5.7 Lateral Displacement of GRS Front Panel

To explore further the response of the hybrid design, the response of the wall's front concrete panel, which is tied to lateral wall pressure in the GRS, was also examined for both a basic GRS and a micropile-GRS construction. The results for both a basic GRS and a hybrid wall in terms of peak and residual deflections of the concrete facing under normal impact are shown in Fig. 5.31. At the bottom part of wall panel, the lateral displacements of the GRS walls with or without micropiles are similarly small. However, the lateral movement of the wall panel of the basic GRS wall under impact is much more significant than that of the hybrid wall in the top region. This reflects the fact that a GRS wall is a more deformable structure especially at the top where the impact occurs. Because of the reinforcement of the micropiles, in contrast, the lateral deflection of the wall panel of hybrid micropile-A-frame-GRS wall is minimal along the whole height of the wall. Such performance will likely reduce the repair and long-term maintenance costs for not only the barriers but also the wall system. For TL-4 impact, the barrier base displacement for the case is 8.6 cm (3.4") for a basic GRS. With the A-frame design, the barrier's base movement is reduced to only 0.67 cm (0.26") under TL-4 impact, illustrative of the increased stiffness of the wall system.



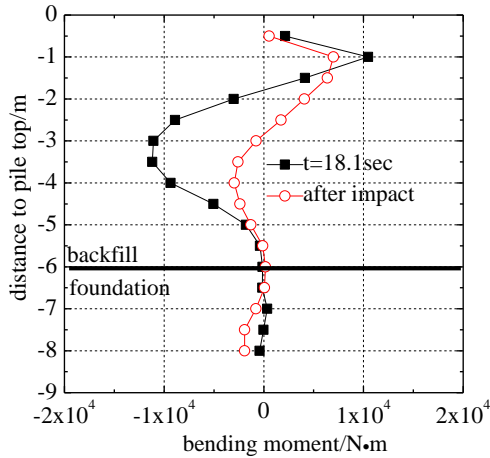
(a) Basic GRS wall (unreinforced)

(b) Hybrid A-frame micropile/GRS wall

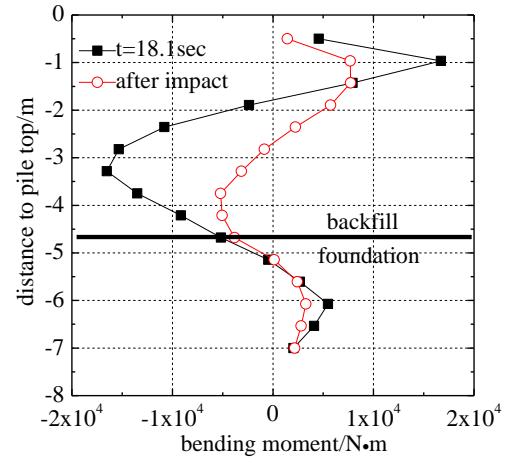
**Figure 5.31: Lateral displacement of residual wall panel induced by different front impact loading**

### 5.8 Bending Moment and Axial Load in Micropiles under Impact

As useful information for the design of the micropile A-frame, the impact-induced bending moments in the vertical and inclined micropiles due to the factored 600 kN dynamic force in the A-frame GRS wall are shown in Fig. 5.32. The peak incremental bending moment of vertical micropile due to the impact is 111.8 kN-m, while the peak bending moment of inclined micropile due to impact is 165.3 kN-m. Overall, their variations along the length are similar. At both pile tops, the incremental bending moments are relatively smaller due to the restraint provided by the grade beam. Going down the piles, the bending moments rise to their peaks rapidly and then decrease, followed by inflection points where the bending moment is zero. Further down the piles, both bending moment curves exhibit a parabolic form and peak at about 3 m below the pile top and in the GRS region. The second inflection point comes into being near the interface between backfill and foundation soil. In the underlying foundation for the vertical pile, the incremental bending moment of the vertical micropile is relatively minor. This is in contrast to the case of the inclined micropile. On the axial load in the piles, the results are plotted in Fig. 5.33 where positive represents tension and negative is compression. Under the outward impact, the vertical pile is, as expected, mainly under compression while the inclined micropile is under tension. The maximum axial force occurs inside the GRS region at 2 or 3 m down from the pile top as well. After the impact loading, the incremental axial force decreases significantly in both piles, with it being almost zero for the inclined pile. These results illustrate the stiffening effect from the micropiles and their ability to defuse the concentration of impact effect on the deformable GRS region.

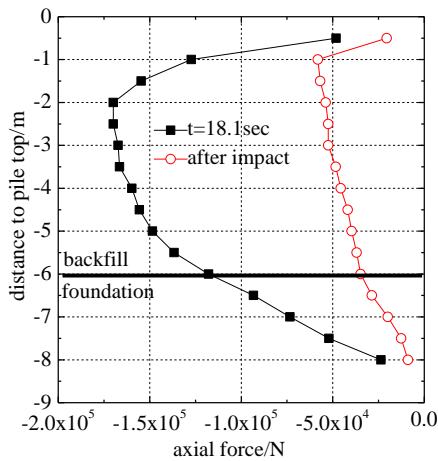


(a) Bending moment of vertical micropile

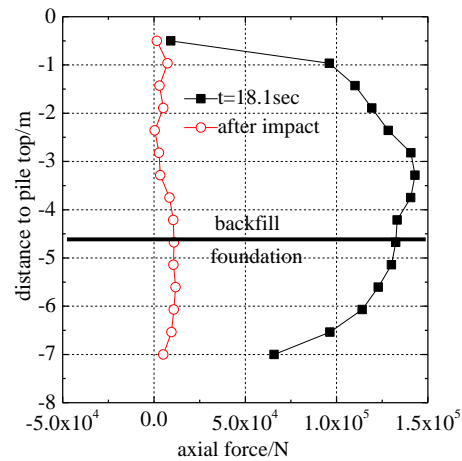


(b) Bending moment of inclined micropile

**Figure 5.32: Bending moment of micropiles induced by 600 kN impact loading in the hybrid A-frame micropile/GRS wall.**



(a) Incremental axial force of vertical pile



(b) Incremental axial force of inclined pile

**Figure 5.33: Axial force of piles induced by 600 kN impact loading**

## 5.9 Grade Beam

The grade beam in the hybrid A-frame micropile-GRS wall is connected not only to the vertical and inclined micropiles, but also to all other A-frames along the roadway to form a longitudinally regular structure. Fig. 5.34 shows the bending moment of grade beam as a result of a 600 kN frontal impact in the hybrid A-frame micropile-GRS wall. The incremental bending moment of the grade beam reaches the peak value of 230.7 kN-m at  $t=0.10$  sec during impact. Away from the action point, the bending moment decreases rapidly, leading first to a point of inflection, and then diminishes to 0. After impact loading, the incremental bending moment exhibits similar trend

but at a much lower level. Fig. 5.35 shows a comparison of the deflection of the grade beam upon impact. One can see that 4 to 5 barriers on each side are affected by the impact loading in the example. As expected, the impact loading is transferred not only from the top to the foundation through the micropile A-frame nearest to the impact, but also sideways to the adjacent barriers. The deformation of barrier under 20° oblique impact loading exhibits similar trends although the deformation of barrier is no longer symmetric as noted earlier.

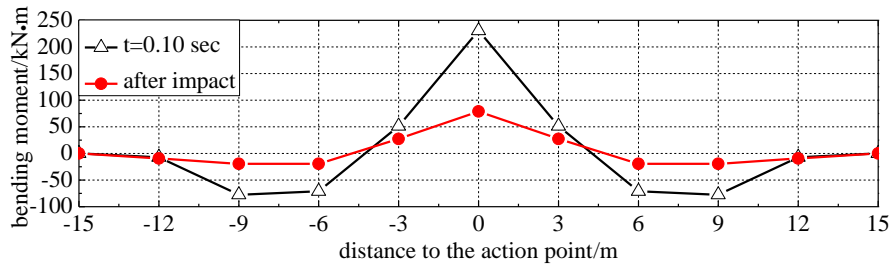


**Figure 5.34: Bending moment of grade beam induced by 600 kN front impact loading**

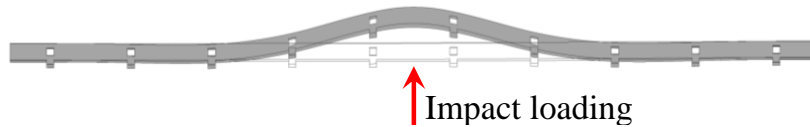


**Figure 5.35: Deformation of grade beam before and after front impact (scale magnified by 50 times)**

### 5.10 Soil Deformation in GRS Region

To visualize the state of deformation in the soil regions, a plot of the spatial distribution of the von Mises or *effective strain* as defined by

$$\varepsilon_{\text{effective}} = \frac{\sqrt{2}}{3} \sqrt{(\varepsilon_1 - \varepsilon_2)^2 + (\varepsilon_2 - \varepsilon_3)^2 + (\varepsilon_3 - \varepsilon_1)^2}$$

where  $\varepsilon_i$  are the principal strains is often helpful as the effective strain is a scalar measure of the magnitude of the deviatoric or shear component of the strain state of the soil medium. The effective strain contours for the GRS region with different internal friction angles of the backfill soil under self-weight are shown in

Fig.5.36. When the backfill soil's strength is well compacted (e.g.,  $\phi=40^\circ$ ), one can see that the effective strain in an ordinary truncated GRS wall is only slightly higher than that of the micropile-GRS wall under self-weight. The difference can become substantial, however, when the backfill soil is weak or suffers a loss of strength due to other events. For the case of  $\phi=20^\circ$ , for example, one can see a clear band of intense effective strain in the backfill of the truncated GRS wall appears, constituting as a potential shear zone and failure mechanism. In contrast, the effective strain field in the backfill of a micropile-GRS wall is much more moderate and stable even in such an extreme case, illustrating the hybrid design's potential in reducing the level of deformation in the whole GRS region.

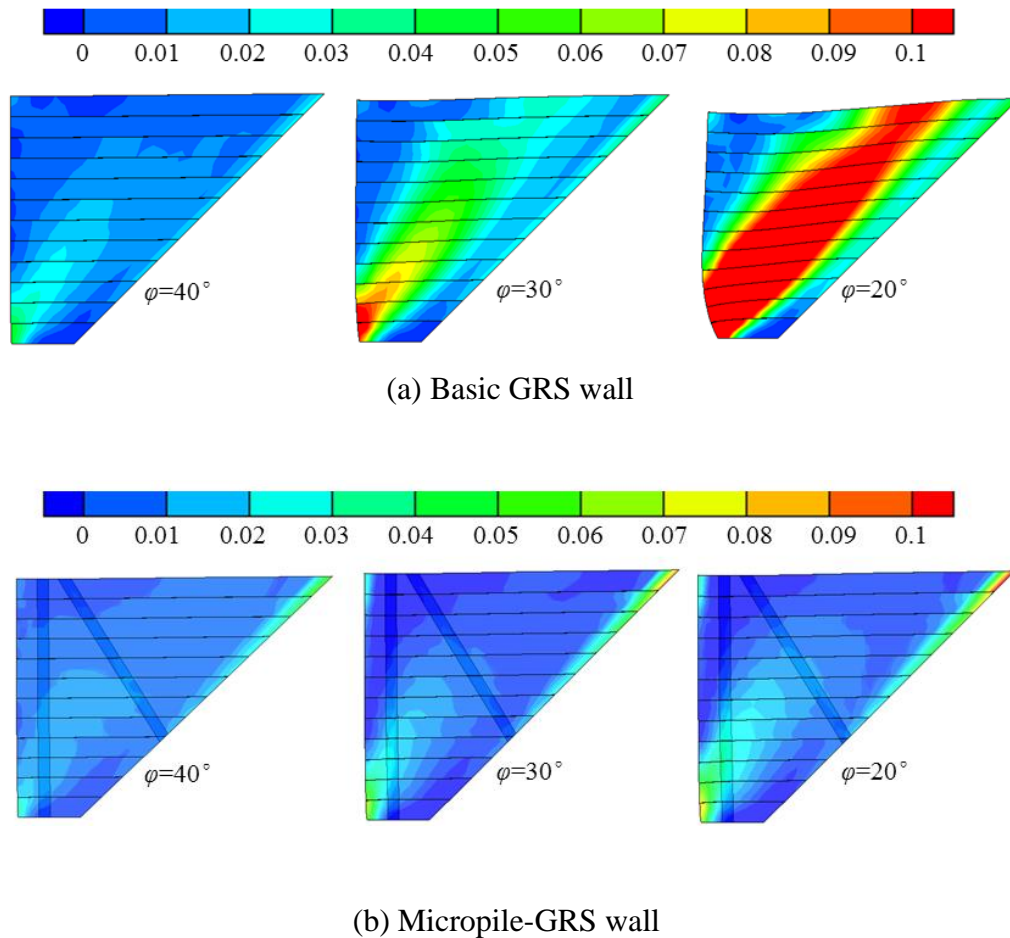


**Figure 5.36: Comparison of equivalent strain in backfill region**

### 5.11 Factor of Safety and Stability of GRS and GRS-Micropile Wall on Soil Slope

For the case of a soil slope instead of rock upon which a truncated GRS is built, the sizable mass of the truncated GRS that is to bear on the slope can lead to a reduction of the local stability of the

slope, a critical concern. With the incorporation of micropiles as a part of the hybrid wall design, however, opportunities for an integrated or dual-purpose solution by using larger micropiles and deeper penetration into the slope are naturally present as mentioned earlier. To quantify the possible improvement in the local factor of safety of the slope by means of the size, spacing and embedment depth of the micropiles in the hybrid design, the method of shear strength reduction (SSR) and large-deformation finite element modeling were used in tandem in this study. As discussed earlier in Section 3, the SSR method involves finding a set of reduced or marginal Mohr-Coulomb material parameters (e.g., through a reduction of the nominal strength parameter(s) by a reduction factor  $\eta_s$ ) that can cause impending failure. In the past, the lack of numerical convergence in infinitesimal-strain finite element solutions has been frequently taken to correspond to physical failure or instability. Apart from its ad hoc theoretical basis and dependence on the numerical and discretization schemes employed, such an approach is not usable with sophisticated finite element codes such as LS-DYNA whose more general finite-strain continuum mechanics formulation will converge to an equilibrium solution even with severe deformation and distortion when those by small-strain theory cannot. To resolve such difficulties so that stability and collapse assessment can be conducted by LS-DYNA, the method of ‘*threshold effective strain*’ developed by Pak [34] was employed. In essence, the method involves the following steps:

- (a) Calibration of the finite element solution using a known or accepted solution that gives a trusted/accepted factor of safety  $FS_{-ref}$  as a reference (it can be from a limit equilibrium (LE) solution such as Morgenstern and Price’s for a homogeneous slope by Slope/W or a relevant benchmark experimental case) of a related problem (e.g., the bearing capacity of a sloping foundation).
- (b) Use the reciprocal of  $FS_{-ref}$  as the *shear strength reduction factor*  $\eta_{s-ref}$  for the same soil condition and geometry and perform a finite element analysis with an appropriate mesh design.
- (c) Search for the effective strain level by which a failure mechanism (e.g. a shear band that clearly isolates one part of the soil body from the other) first emerges in the backfill and/or slope regions and define that critical strain level as “*threshold effective strain*  $\varepsilon_{threshold}$  .”
- (d) Use the threshold effective strain as defining the failure strain level and perform FE analyses of other pertinent configurations of interest by the same finite element mesh or one with a comparable density for a range of reduction factor  $\eta_s$  and its associated reduced soil’s strength parameters.

(e) Find the value  $\eta_{s-crit}$  which is the highest  $\eta_s$  in (d) that leads to the first emergence of a failure mechanism in the soil.

(f) Define the factor of safety (FS) against slope failure as  $1/\eta_{s-crit}$ , i.e.,

$$FS = 1/\{\eta_{s-crit}\} \text{ where } \eta_{s-crit} = \tan(\phi_{marginal})/\tan(\phi_{nominal}) = c_{marginal}/c_{nominal}.$$

In the context of the Geological Cap model and its shear strength parameter  $\theta$ , one can determine the Factor of Safety by

$$FS = \frac{1}{\eta_s} = \frac{\tan(\varphi_{nominal})}{\tan(\varphi_{marginal})} = \frac{\tan(\sin^{-1} 3\theta_{nominal})}{\tan(\sin^{-1} 3\theta_{marginal})}$$

where  $\theta_{marginal} = \eta_{s-crit} * \theta_{nominal}$ , in the Geological Cap model by virtue of Eqn. (20) which relates  $\varphi$  to  $\theta$ .

Using the SSR method in combination with the threshold-strain definition as outlined, the factors of safety using LS-DYNA regarding the possibility of wall-slope failure under the action of a truncated GRS wall with and without micropiles were computed and illustrated in Fig. 5.37 to 5.39 under gravity and surcharge loads. As can be seen from the displays, the GRS-micropile design can increase the overall factor of safety of the GRS-slope from 1.07 to above 1.3 with a micropile size of 10” instead of 9” (as in Fig. 5.12) at a spacing of 3m (10 ft.) and 2.5m (8 ft.) of pile penetration into the slope. From the displays, one may also notice that the thickness of the slip zone in the foundation region with micropiles is larger than the one in the pure GRS case due to the 2.5m penetration and reinforcement by the micropiles.

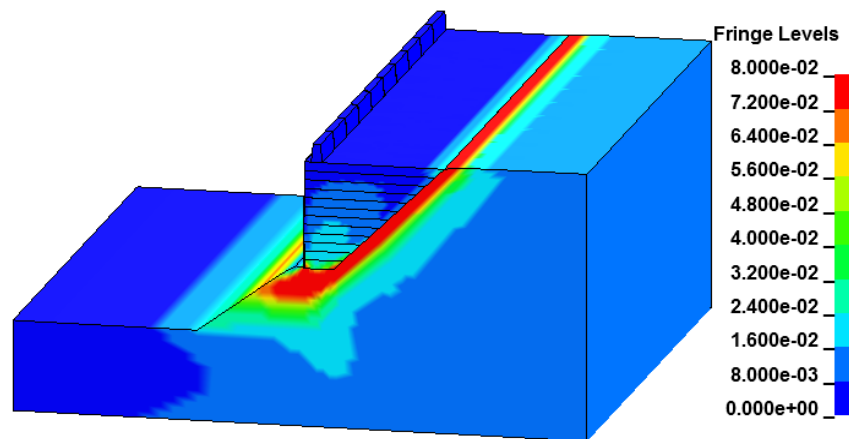


**Figure 5.37: Effective strain contour of 30m basic GRS in Stage II: foundation  $\theta_{marginal} = 0.205$  or  $\varphi = 38^\circ$  (Fs=1.07)**

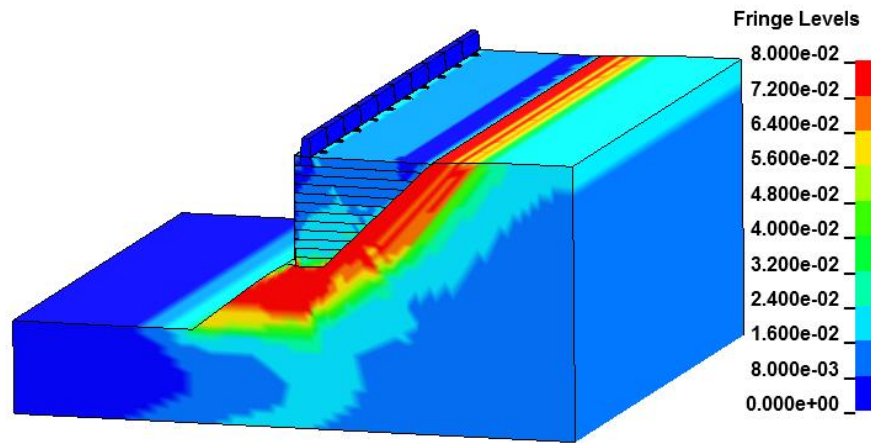


**Figure 5.38: Effective strain of 30m GRS-micropile case with 2.5m pile anchorage in Stage II: foundation  $\theta_{\text{marginal}}=0.176$  ( $F_s=1.328$ ),  $E_{\text{pile}}=14\text{GPa}$  (10")**

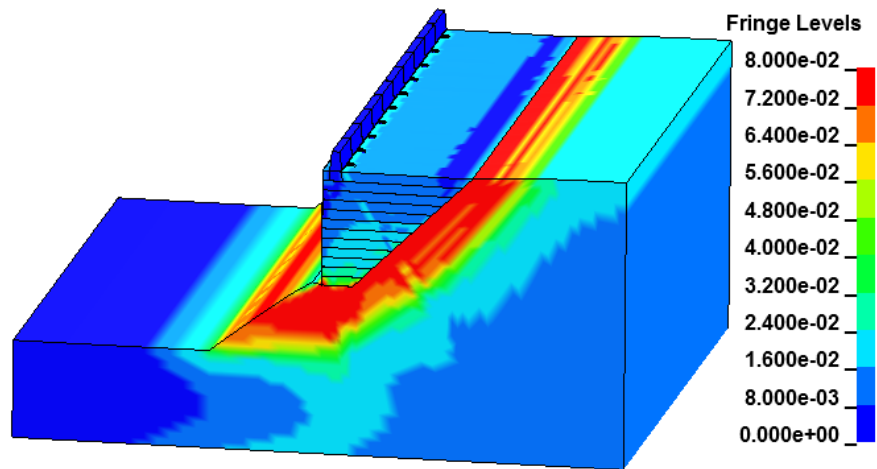


**Figure 5.39: Effective strain of 30m GRS-micropile case with 2.5m pile anchorage in Stage II: foundation  $\theta=0.176$  ( $F_s=1.36$ ),  $E_{\text{pile}}=14\text{GPa}$  (10")**

For Stage III-impact loading at 240 kN, the difference in responses from a basic GRS and a A-frame micropile-GRS system is illustrated in Fig. 5.40-5.44. Under the impact load, the basic GRS without micropiles shows significant local deformation, whereas the micropile A-frame system can handle the dynamic load with a comfortable margin. Close-ups of the conditions are shown in Fig. 5.42 and 5.44. A comparison of the impact response of the truncated GRS and one with 9" or 10" micropiles can be found in Fig. 5.45 to 5.47.

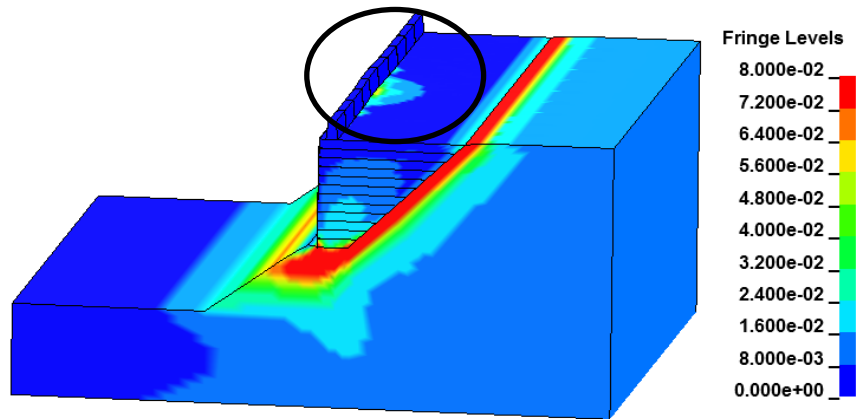


**Figure 5.40: Effective strain of 30m basic GRS in Stage III:  
foundation  $\theta_{\text{marginal}}=0.205$  ( $F_s=1.076$ )**

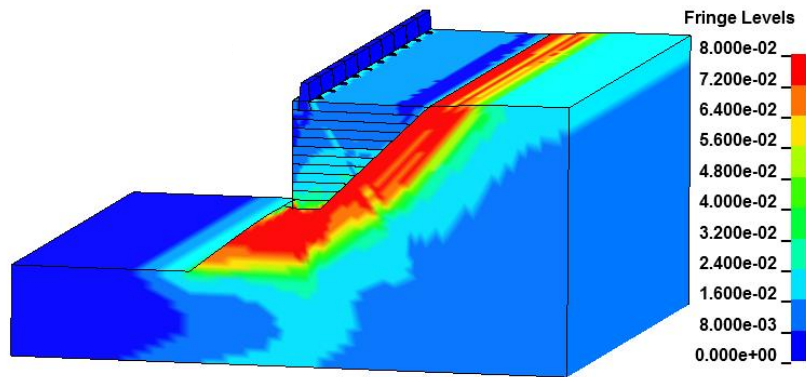


**Figure 5.41: Effective strain of 30m GRS-micropile case with 2.5m pile anchorage in Stage III: foundation  $\theta_{\text{marginal}}=0.176$  ( $F_s=1.35$ ),  $E_{\text{pile}}=14\text{GPa}$  (10")**

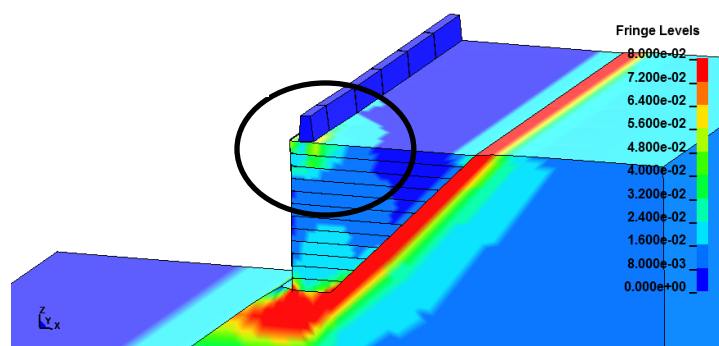


**Figure 5.42: Effective strain of 30m basic GRS in Stage III: foundation  $\theta_{\text{marginal}} = 0.205$  ( $F_s = 1.076$ ), Mid-plane**

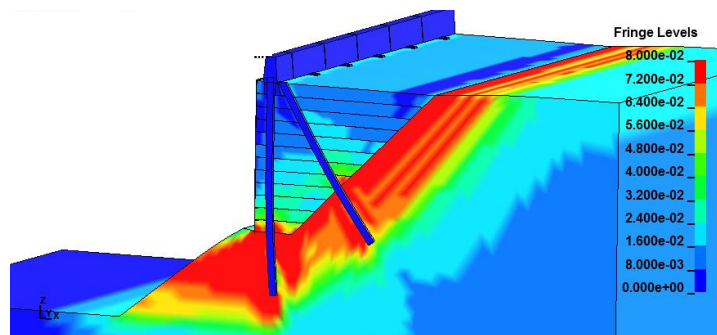


**Figure 5.43: Effective strain of 30m micropile case with 2.5m pile anchorage in Stage III: foundation  $\theta_{\text{marginal}} = 0.176$  ( $F_s = 1.35$ ),  $E_{\text{pile}} = 14\text{GPa}$  (10”), Mid-plane**

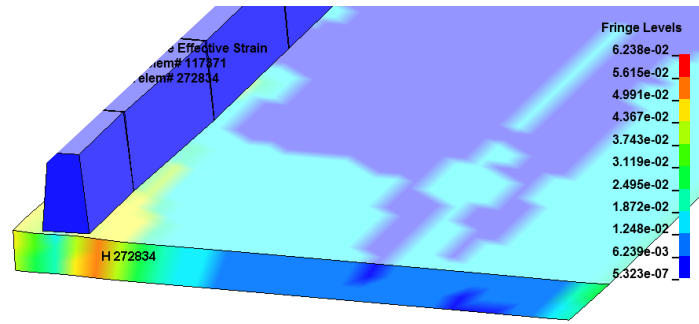


**Figure 5.44: Effective strain near barrier of 30m basic MSE in Stage III: foundation  $\theta_{\text{marginal}} = 0.205$ ,  $F_s = 1.076$ , Mid-plane, max=6.2% in front of barrier**

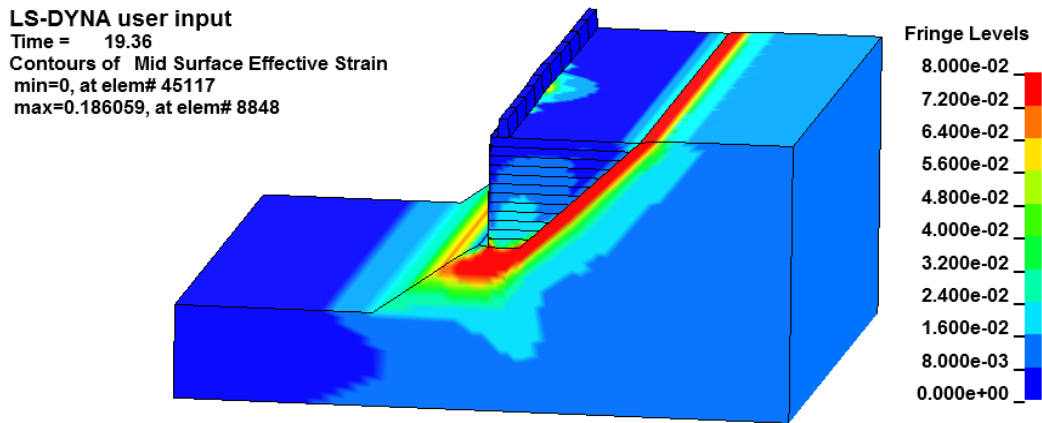


**Figure 5.45: Effective shear strain contour of 30m basic MSE in Stage III-dynamic: foundation  $\theta_{\text{marginal}} = 0.205$  ( $F_s = 1.07$ )**

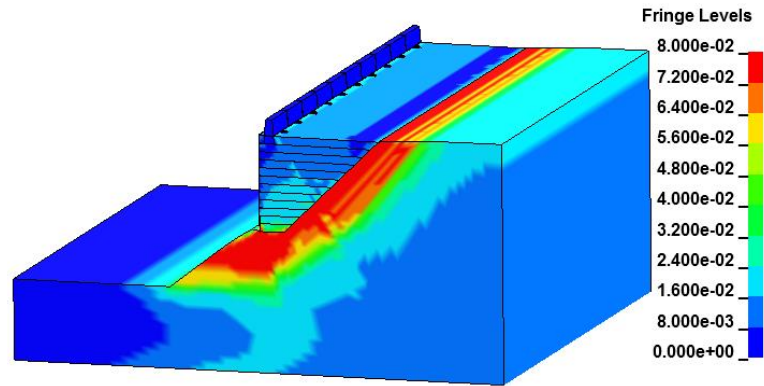


**Figure 5.46: Effective strain of 30m MSE- GRS pile case Stage III-dynamic,  $E_{pile}=12\text{GPa}$  (9'') 0, 2.5m anchorage, 2.5m anchorage, foundation  $\theta_{\text{marginal}}=0.176$  (Fs=1.33)**

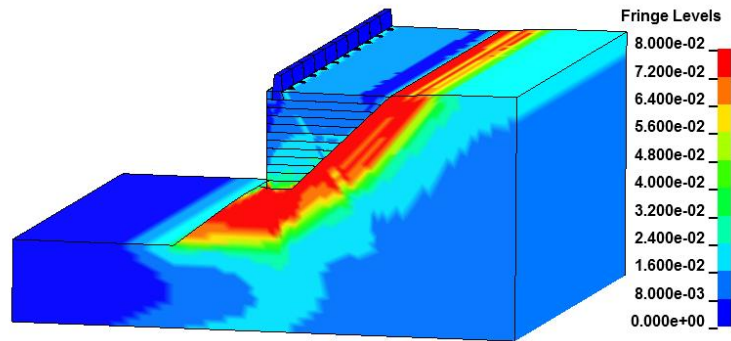


**Figure 5.47: Effective strain of 30m GRS pile case in Stage III-dynamic,  $E_{pile}=14\text{GPa}$  (10''), 2.5m anchorage, foundation  $\theta_{\text{marginal}}=0.176$  (Fs=1.35)**

### 5.12 Parametric Variation of Design Parameters in Hybrid Micropile A-Frame-GRS Walls

To provide some quantitative information about the effectiveness of various design options for a truncated GRS wall with micropile A-frames, parametric studies were conducted to determine the influence of pile size, pile penetration depth into the slope and the A-frame spacing on the overall factor of safety for a slope under the loading of the truncated GRS wall. With the same reference GRS geometry and shear strength parameter of the soil in the reference slope stability problem depicted in Fig. 5.48 for which a factor of safety of 1.159 was obtained by SLOPE/W as  $FS_{\text{-ref}}$  and matched by the project's LS\_DYNA solution using the threshold strain method (see Fig. 5.49), 3 sets of results for design usage are shown in Fig. 5.50, 5.51 and 5.52, respectively. Using a 12'' micropile size ( $E_{pile}=25\text{GPa}$ ), 2.5m pile penetration and 3m spacing as the reference case upon which each engineering option was varied, one can see for instance from Fig. 5.51 and 5.52 that

an increase in the pile size or pile embedment into the foundation can indeed increase the Factor of Safety effectively. Likewise, one can find the sensitivity of FS to the spacing between the A-frames as well. Among the 3 options, it appears that increasing the depth of penetration of the micropiles is the most effective among these basic options for the wall-slope configuration.

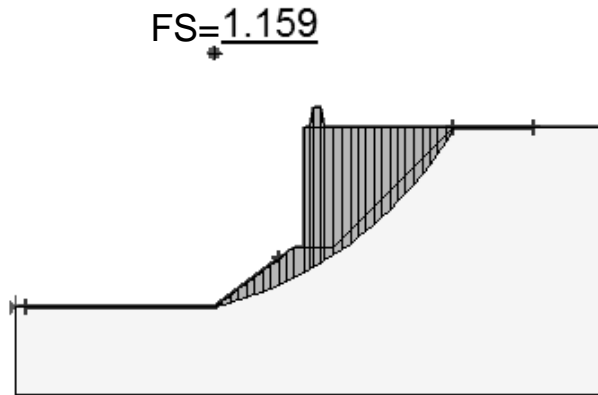


**Figure 5.48: FS of basic GRS-slope model by LE solution via SLOPE/W**

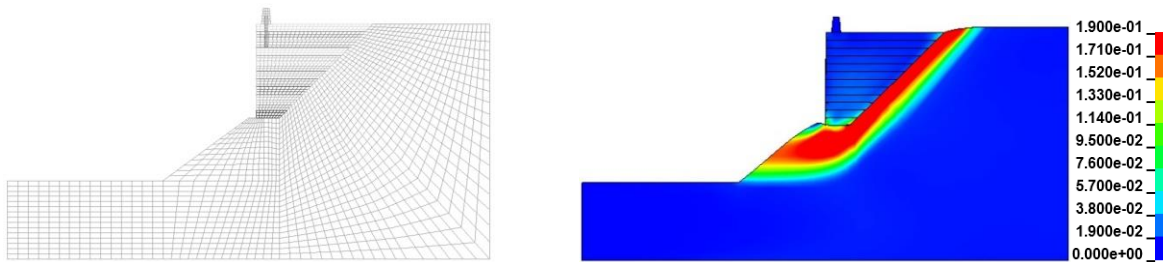
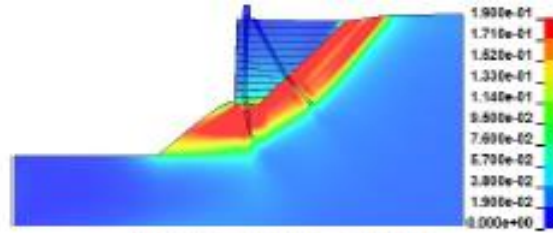
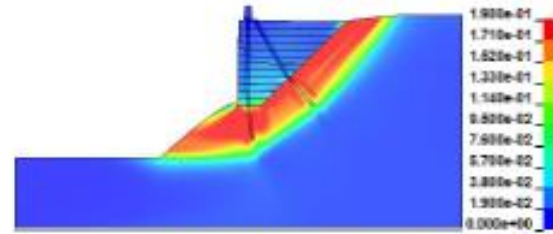


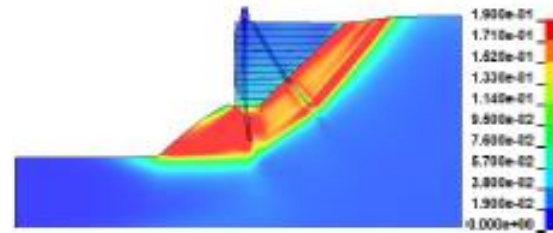
**Figure 5.49: Threshold strain of basic GRS-slope model @ 19% for FS =1.159 by finite element solution**



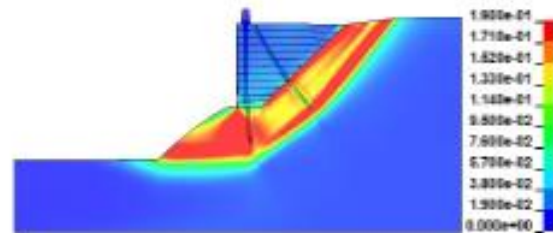
(b) Epile =2.5 GPa: FS=1.338



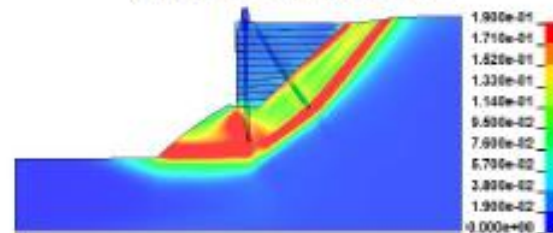
(c) Epile =5 GPa) : FS=1.409



(d) Epile =10 GPa) : FS=1.497

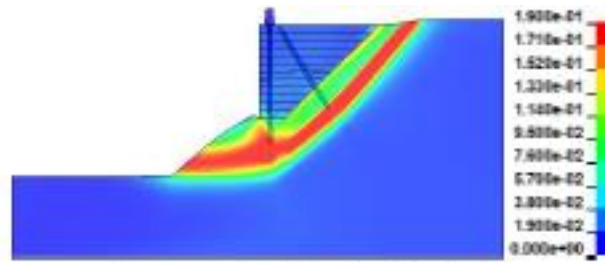


(e) Epile =15 GPa) : FS=1.525

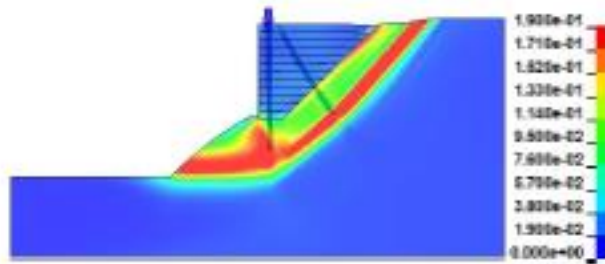


(f) Epile =25 GPa) : FS=1.565

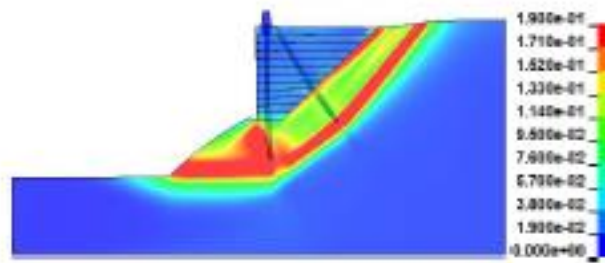
**Figure 5.50: FS and equivalent strain distribution of GRS with different pile modulus/size**



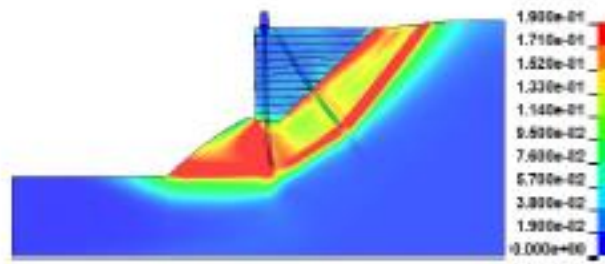
(b) penetration=1.5 m) : FS=1.397



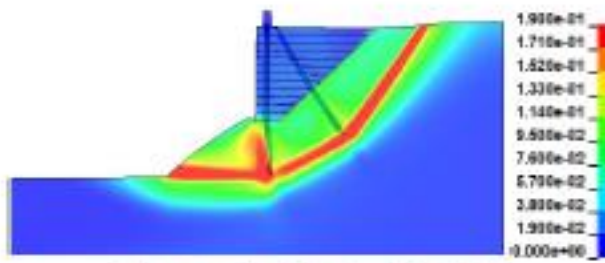
(c) penetration =2 m) : FS=1.459



(d) penetration=2.5 m) : FS=1.565

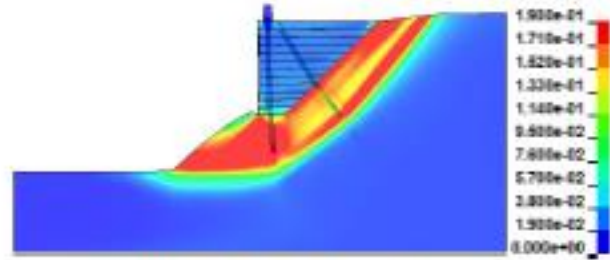


(e) penetration=3 m) : FS=1.682

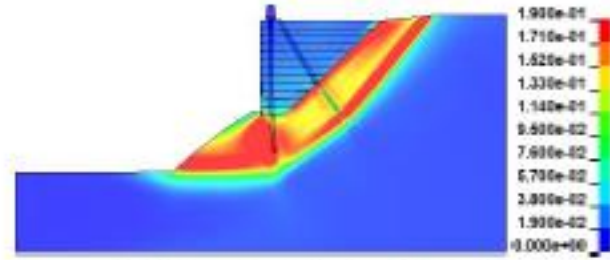


(f) penetration=3.5 m) : FS=1.828

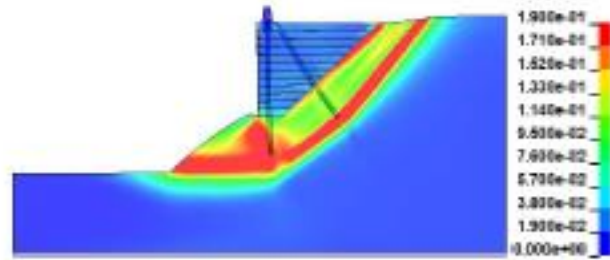
**Figure 5.51: FS and equivalent strain distribution of GRS with different pile penetration depth**



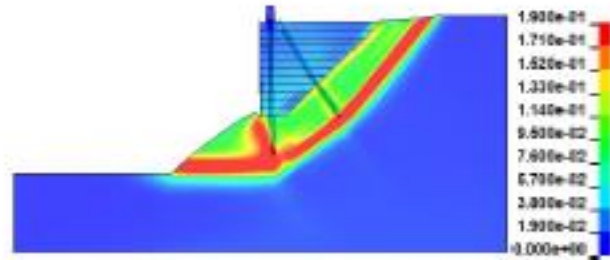
(b) pile spacing=4 m : FS=1.380



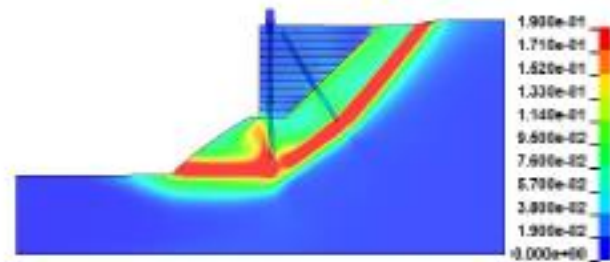
(c) pile spacing=3.5 m : FS=1.460



(d) pile spacing=3 m : FS=1.565



(e) pile spacing=2.5 m : FS=1.610



(f) pile spacing=2 m : FS=1.667

**Figure 5.52: FS and equivalent strain distribution of GRS with different A-frame spacing**

# 6 TRANSLATION OF RESEARCH TO ENGINEERING PRACTICE

The results from this study have been employed by CDOT in developing preliminary engineering worksheets for field implementation of the hybrid micropile A-frame-GRS wall design. Examples are Worksheet\_B-504-A3, A5 and V2 shown below. To minimize the risk of crack formation as a result of settlements of the fill and foundation soils relative to the micropiles, the determination of a practical waiting period (by field monitoring or settlement analysis) before completing the construction of the grade beam and pavement is advisable. Suitable physical test sections and more detailed mechanics modeling to detect and resolve other potential engineering aspects that may affect field performance is also recommended.

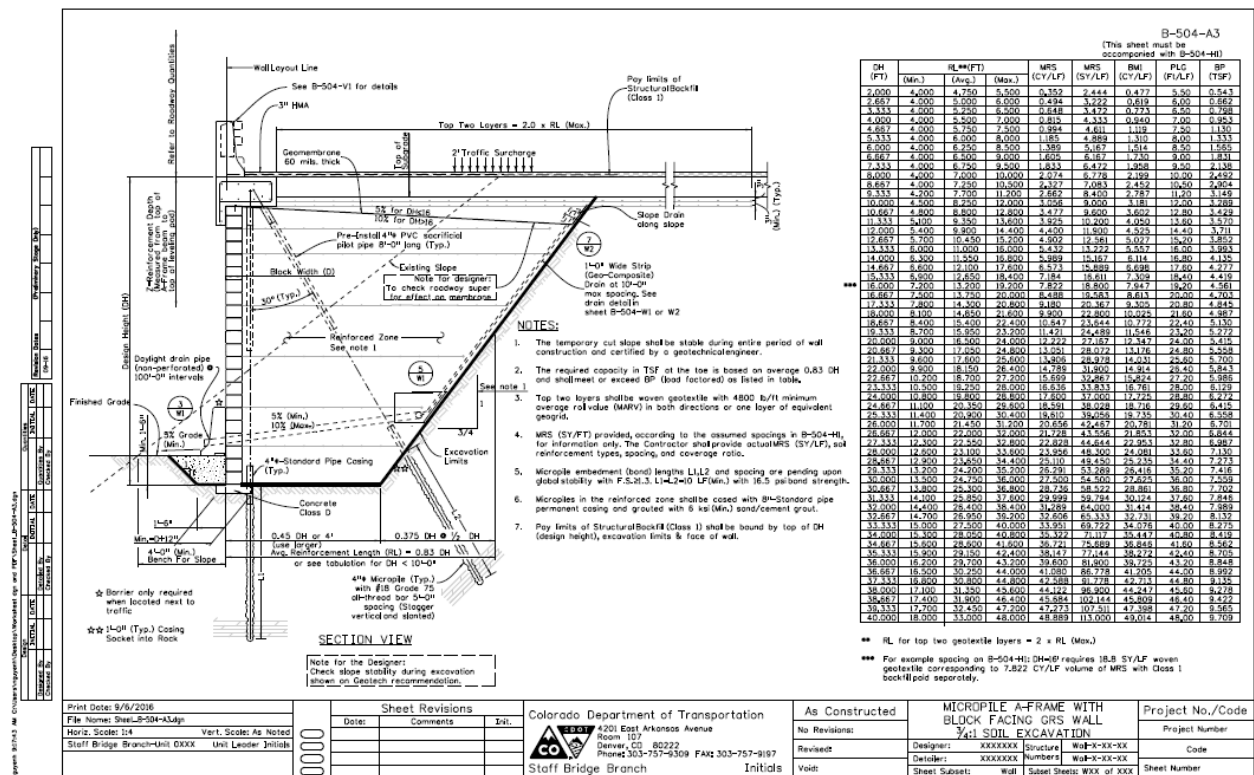
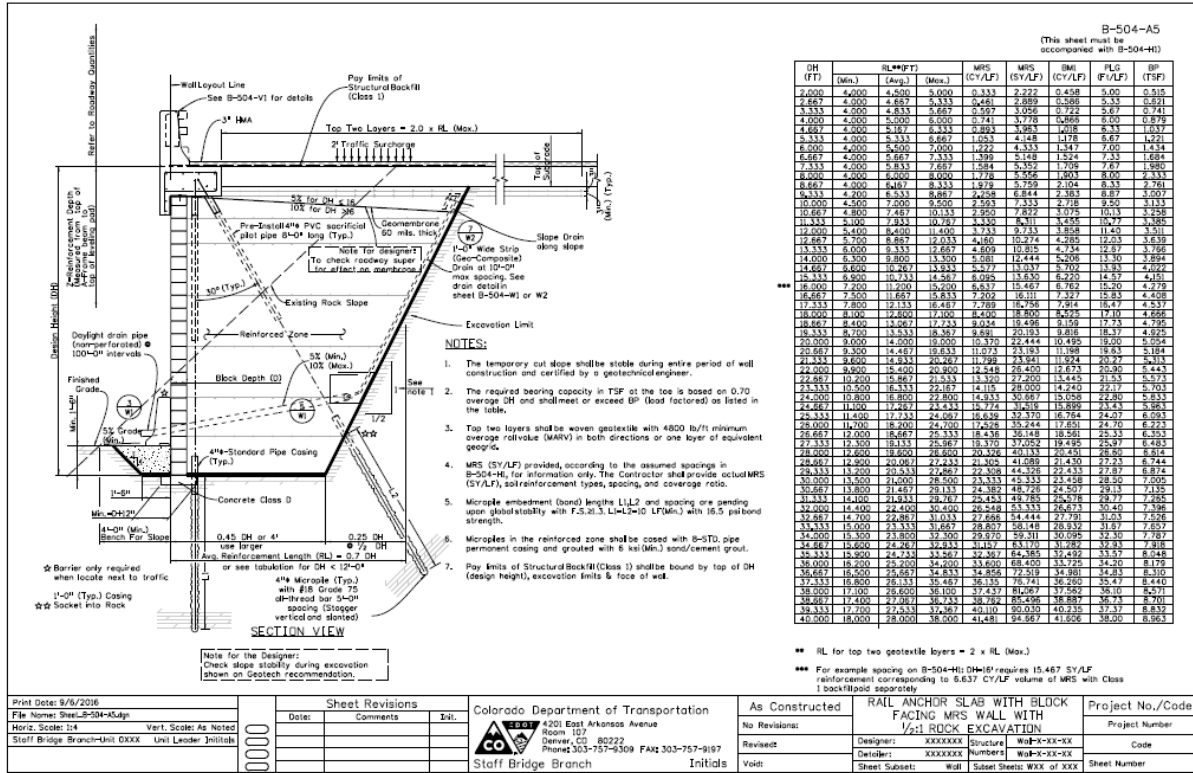


Figure 6.1: CDOT Worksheet\_B-504-A3



## 7 SUMMARY AND CONCLUSIONS

Taking into consideration of the inconvenience and danger in construction, the complexity in the loading condition and restricted layout of GRS walls in mountainous areas or on steep slopes, the idea of installing a pair of vertical and inclined micropiles in the form of a A-frame into the GRS as a hybrid wall-barrier system was investigated in this project. To evaluate the design's merit and potential, extensive numerical simulations of the design under gravity, surcharge and impact loading were conducted by 3D elastoplastic finite element modeling using LS-DYNA. Collaborated partially by an experimental scaled model study of the adopted numerical modeling platform, the performance of the hybrid design under self-weight, surcharge and impact loads was investigated and compared with that of a truncated GRS wall with regular construction. Detailed response information on its material components such as soil, micropile, geotextile, barrier and slope in nominal and limit states were both considered. While there are additional practical engineering aspects to be explored and more realistic representations of the material components can be incorporated, the study has shown that the hybrid design offers a promising alternative that allows truncated GRS to be more commonly used not only with impact barriers but also on marginal soil conditions that are often encountered in mountainous areas and steep terrains. With careful design and field implementation, the approach can potentially reduce costly and dangerous earthwork compared to past approaches while meeting the requisite standard of safety and performance.

## 8 REFERENCES

- [1] Ross HE, Sicking, DL, Zimmer RA , Michie JD, Recommended Procedures for the Safety Performance Evaluation of Highway Features, NCHRP Report 350, 1993
- [2] Tom Armour, P.E., Paul Groneck, P.E., James Keelev, Sunil Sharma. “Micropile Design and Construction Guidelines, Priority Technologies Program (PTP) Project” FHWA-SA-97-070, 2000.
- [3] Wu, JTH, Lee KZZ, Helwany SB, Ketchart, K, Design and Construction Guidelines for Geosynthetic-Reinforced Soil Bridge Abutments with a Flexible Facing, NCHRP REPORT 556, 2006
- [4] Morrison KF, Harrison F.E, Collin JG, Dodds A, Arndt B, Shored Mechanically Stabilized Earth (SMSE) Wall Systems Design Guidelines, Publication No. FHWA-CFL/TD-06-001 February 2006.
- [5] Bligh RP, Briaud JL, Kim KM, Abu-Odeh, A, Design of Roadside Barrier Systems Placed on MSE Retaining Wall, NCHRP Project 22-20 Report 663, 2010.
- [6] Elias, V, Christopher, BR, Berg RR “Mechanically Stabilized Earth Walls and Reinforced Soil Slopes Design and Construction Guidelines,” FHWA-NHI-00-043, NHI course No. 132042 March 2001.
- [7] Chang NY, Oncul F, Three-dimensional load transfer of Colorado Type 7 ad Type 9 rails on independent moment slab under high test level impact, Report No. CDOT-DTD-R-2003-2, Final Report, 2004.
- [8] Design and Construction of Mechanically Stabilized Earth Walls Reinforced Soil Slopes, FHWA Geotechnical Engineering Circular No. 11, Shored Mechanically Stabilized Earth (SMSE) Wall Systems Design Guidelines, FHWA-CFL/TD-06-001
- [9] Morrison K., Harrison F., Collin, J., Dodds, A. & Arndt, B. (2006). Shored mechanically stabilized earth (SMSE) wall systems. FHWA-CFL/TD-06-001.
- [10] Wu, JTH, Lee KZZ, Helwany SB, Ketchart, K, Design and Construction Guidelines for GRS Bridge Abutments with a Flexible Facing: Appendix C—Verification of the Analytical Mode,” NCHRP Web-Only Document 81 (Project 12-59): Contractor’s Final Report, 2004.
- [11] Lee ZZ, Geosynthetic-reinforced soil walls under multi-directional seismic shaking, Ph.D. thesis, Univ. of Colorado, Denver, 2011.
- [12] Kang MK, Design of roadside barrier systems placed on mechanically stabilized earth (MSE) retaining walls, Ph.D. thesis, Texas A&M University, 2009.
- [13] Aryal KP, Differences between LE and FE Methods used in Slope Stability Evaluations,” 12th International Conference of International Association for Computer Methods and Advances in Geomechanics (IACMAG), 1-6 October, 2008, Goa, India, 4590-4516.
- [14] Aryal, K. (2006): Slope stability evaluation by LE and FE methods . Ph D thesis, Norwegian University of Science and Technology, NTNU: Electronic version: <http://www.diva-portal.org/ntnu/abstract.xsql?dbid=1868>.
- [15] Abramson, L. W., Lee, T. S., Sharma, S., and Boyce, G. M. (2002). Slope Stability Concepts. Slope Stabilisation and Stabilisation Methods, Second edition, published by John Willey & Sons, Inc., pp. 329-461.
- [16] SLIDE (2003). Stability analysis for soil and rock slopes. Slide, User’s Guide, Geomechanics Software Solutions, Rocscience , Inc., Canada. [www.rocscience.com](http://www.rocscience.com)
- [17] SLOPE/W (2002). Stability Analysis. Users Guide Version 5, GeoSlope Office, Canada. [www.geoslope.com](http://www.geoslope.com).
- [18] Bligh, R.P., Sheikh, N.M., Alberson, D.C., and Abu-Odeh, A.Y. (2005). Low Deflection Portable Concrete Barrier. TXDoT
- [19] Collin, J.G. (2004). “Lessons learned from a segmental retaining wall failure.” Geotextiles and Geomembranes. 19(7), 445-454.
- [20] Parsons, R. L., Pierson, M. C., Han, J., Brennan, J. J., and Brown, D. A. —Lateral load capacity of cast-in-place shafts behind an MSE wall. ASCE Geotechnical Special Publication No. 186, p. 560-567, IFCEE 09’ 2009a.

- [21] Pierson, M. C., Parsons, R. L., and Han, J. —Modeling of MSE wall – drilled shaft systems, . Proc. 34th Annual Conference on Deep Foundations, DFI, 2009.
- [22] Pierson, M. C., Parsons, R. L., Han, J., Brown, D. A., and Thompson, R. W. —Capacity of Laterally Loaded Shafts Constructed behind the Face of a Mechanically Stabilized Earth Block Wall.|| Final Report, Kansas Department of Transportation, 81pages, <http://www.ksdot.org/PublicLib/publicDoc.asp?ID=003782466>, 2008.
- [23] Berg R and Volova, C, (2001) Effects of *Pile Driving Through a Full-Height Precast Concrete Panel Faced Geogrid-Reinforced Mechanical Stabilized Earth (MSE) Wall*, *ascelibrary.org/doi/pdf/10.1061/40903(222)3*.
- [24] Amoco Geotextile ProPex 2044 Specs, Amoco Fabrics and Fibers Company, Austell, GA 30168
- [25] Scott RF, Principles of Soil Mechanics, Addison-Wesley Publ. Co. 1963.
- [26] Zienkiewicz, O. C., Humpheson, C., and Lewis, R. W., 1975, “Associated and Non-Associated Visco-Plasticity and Plasticity in Soil Mechanics,” *Geotechnique*, Vol. 25, No. 4, pp. 671-689.
- [27] Duncan, J.M., State of the art: limit equilibrium and finite-element analysis of slopes, *Journal of Geotechnical Engineering*, vol. 122, no. 7, pp. 577-596. 1996.
- [28] Griffiths, D.V. and Lane, P.A., Slope stability analysis by finite elements, *Geotechnique*, vol. 49, no. 3, pp. 387-403. 1999
- [29] Chang YL, Huang TK, Slope stability analysis using strength reduction technique, *Journal of the Chinese Institute of Engineers*, Vol. 28, No. 2, pp. 231-240 (2005).
- [30] Li, H. and Shao, L. (2011) Three-Dimensional Finite Element Limit Equilibrium Method for Slope Stability Analysis Based on the Unique Sliding Direction. *Slope Stability and Earth Retaining Walls*: pp. 48-55. doi: 10.1061/47627(406)
- [31] Tensor Earth Technologies, —Demonstration of pile driving through the HDPE geogrid reinforced soil fill of full-height precast concrete panel faced, mechanically stabilized earth wall, Report, Colorado E-470 Project, 2001.
- [32] LS-DYNA user’s manual, Vol. III, Version 960, Livermore Softw. Tech. Corp., March 2001.
- [33] Zhang, ZC (2015), “Study on deformation and stability of highway Micropile-MSE (Mechanically Stabilized Earth) retaining walls in mountainous areas ,” Ph.D. dissertation, Hohai University, China, 2015.
- [34] Pak, R.Y.S. Hybrid MSE-Micropile-Barrier-Slope Analysis and Design Phase II-Progress presentation, PPT presentation to CDOT, Aug 2015.
- [35] DiMaggio, F.L., Sandler, I.S. Material model for granular soils. *J. Eng. Mech. Div.*, 1971, 97(3): 935-950
- [36] Hallquist, J.O. . LS-DYNA Keyword User’s Manual (971 R6.0.0)[M]. Livermore:Livermore Software Technology Corporation, 2012.
- [37] Chen, W.F., Saleeb, A.F. Constitutive Equations for Engineering Materials. In: *Elasticity and Modeling*, vol. 1[M]. Amsterdam:Elsevier, 1994.
- [38] Zhang, ZC. Ph.D thesis, Study on the deformation and stability of highway Micropile-MSE (Mechanically Stabilized Earth) retaining walls in mountainous areas, Hohai University, Nanjing, China, 2015.